The Role of Diabatic Heating in the Midlatitude Atmospheric Circulation Response to Climate Change🖉

SOUMIK GHOSH🅾,[a,b] ORLI LACHMY,[b] AND YOHAI KASPI[a]

[a] *Department of Earth and Planetary Sciences, Weizmann Institute of Science, Rehovot, Israel*
[b] *Department of Natural Sciences, The Open University of Israel, Ra'anana, Israel*

ABSTRACT: Climate models generally predict a poleward shift of the midlatitude circulation in response to climate change induced by increased greenhouse gas concentration, but the intermodel spread of the eddy-driven jet shift is large and poorly understood. Recent studies point to the significance of midlatitude midtropospheric diabatic heating for the intermodel spread in the jet latitude. To examine the role of diabatic heating in the jet response to climate change, a series of simulations are performed using an idealized aquaplanet model. It is found that both increased CO_2 concentration and increased saturation vapor pressure induce a similar warming response, leading to a poleward and upward shift of the midlatitude circulation. An exception to this poleward shift is found for a certain range of temperatures, where the eddy-driven jet shifts equatorward, while the latitude of the eddy heat flux remains essentially unchanged. This equatorward jet shift is explained by the connection between the zonal-mean momentum and heat budgets: increased diabatic heating in the midlatitude midtroposphere balances the cooling by the Ferrel cell ascending branch, enabling an equatorward shift of the Ferrel cell streamfunction and eddy-driven jet, while the latitude of the eddy heat flux remains unchanged. The equatorward jet shift and the strengthening of the midlatitude diabatic heating are found to be sensitive to the model resolution. The implications of these results for a potential reduction in the jet shift uncertainty through the improvement of convective parameterizations are discussed.

SIGNIFICANCE STATEMENT: The latitude of the eddy-driven jet displays considerable variation in climate models, and the factors influencing this variability are poorly understood. This work connects the strength of midlatitude diabatic heating to the structure of the midlatitude circulation and the eddy-driven jet latitude. The direction of the eddy-driven jet shift in response to climate change is found to depend on the diabatic heating response, which in turn depends on the parameterized convective heating. These results highlight the role of convective parameterizations in the representation of the midlatitude circulation in climate models. Additionally, the results imply that the eddy-driven jet shift cannot be explained solely based on the storm-track response to climate change, in contrast with previously suggested explanations.

---

1. Introduction

The location and intensity of the midlatitude jet stream and storm track largely determine the structure and properties of the extratropical climate. Climate models from both phases 5 and 6 of the Coupled Model Intercomparison Project (CMIP5 and CMIP6) generally predict a poleward shift of the midlatitude circulation in response to climate change induced by increased greenhouse gas concentration. This shift includes the eddy-driven jet and the midlatitude storm track. Notably, a more robust poleward shift is identified in the Southern Hemisphere than in the Northern Hemisphere (e.g., Chang et al. 2012; Barnes and Polvani 2013; Vallis et al. 2015; Curtis et al. 2020). The intermodel spread of the poleward jet shift in

response to climate change is quite large, with several models showing an equatorward jet shift for certain seasons. The mechanism responsible for the poleward shift of the midlatitude circulation is a subject of ongoing research, and several explanations have been proposed (Shaw 2019 and references therein). Studying the circulation response to climate change using idealized general circulation models (GCMs) with different levels of complexity has progressed the theoretical understanding of this response (e.g., O'Gorman and Schneider 2008a; Butler et al. 2010; Lu et al. 2010; Kidston et al. 2011; Chen et al. 2013; Shaw and Tan 2018; Tan et al. 2019), yet some outstanding questions remain. The focus of this study will be on the role of midlatitude diabatic heating in the midlatitude circulation response to climate change, which has received relatively little attention despite its importance.

Diabatic heating in the midlatitude midtroposphere is dominated by latent heating associated with midlatitude storms, which is partly offset by radiative cooling. Latent heating is generally expected to increase in response to global warming due to moisture increase following the Clausius–Clapeyron relation, but it is also affected by changes in the dynamics (Held and Soden 2006; O'Gorman and Schneider 2008b). Midlatitude diabatic heating was found to enhance the poleward

---

Corresponding author: Soumik Ghosh, soumik.ghosh@fulbrightmail.org, soumik.ghosh@weizmann.ac.il, ghosh.soumik@uqam.ca

deflection of storms in response to warming (Tamarin and Kaspi 2017). Moisture increase in response to climate change was found to account for most of the poleward jet shift, while cloud radiative effects play a secondary role (Tan and Shaw 2020). Recently, Lachmy (2022) found a high correlation between the strength of midlatitude midtropospheric diabatic heating and the latitudinal separation between the eddy heat flux and the eddy-driven jet in the intermodel spread of CMIP6 models. Lachmy (2022) further showed that the responses of eddy heat flux and diabatic heating in CMIP6 models have comparable roles in balancing the momentum source response associated with the poleward jet shift. These studies indicate that midlatitude diabatic heating is an important factor in the midlatitude circulation response to climate change. Taking this factor into account could potentially fill some gaps in the theoretical understanding of this response.

One of the unresolved issues regarding the jet response to climate change is the relation between the eddy-driven jet shift and the shift of the baroclinic zone. Some studies based their explanations for the poleward shift of the eddy-driven jet on a mechanism for the poleward shift of the baroclinic zone and the eddy heat flux, assuming that the eddy-driven jet and eddy heat flux shift together, which is a valid assumption in most cases (e.g., Frierson 2008; Lu et al. 2008; Butler et al. 2011; Voigt and Shaw 2016). In contrast, other studies found that the eddy heat flux shifts poleward in response to climate change, while the eddy-driven jet shifts equatorward in an idealized GCM, under certain conditions (Pfahl et al. 2015; Dwyer and O'Gorman 2017; Lachmy and Shaw 2018; Tan et al. 2019; Davis and Birner 2022). While these opposite shifts depend on the model configuration, and specifically on the radiation parameterization (Tan et al. 2019; Davis and Birner 2022) and convective parameterization (Garfinkel et al. 2024), they indicate that the latitudinal shift of the eddy-driven jet could not be fully explained based on the eddy heat flux shift.

The latitudinal separation between the eddy heat flux and eddy-driven jet was found to be related to the strength of midlatitude midtropospheric diabatic heating in observations and CMIP6 models (Lachmy and Kaspi 2020; Lachmy 2022). As explained in Lachmy and Kaspi (2020), the latitudes of maximum eddy heat flux and eddy-driven jet (defined by the surface westerlies) are collocated if the three following conditions are satisfied:

1) The maximum eddy heat flux is collocated with the maximum Ferrel cell (FC) streamfunction. This condition depends on the heat balance between the eddy heat flux convergence and the adiabatic heating by the Ferrel cell's vertical motion.
2) The maximum Ferrel cell streamfunction is collocated with the maximum near-surface zonal-mean meridional wind. This condition depends on the vertical alignment of the Ferrel cell streamfunction.
3) The maximum near-surface meridional wind is collocated with the maximum surface westerlies. This condition depends on the momentum balance between the Coriolis force and the drag near the surface.

As shown in Lachmy and Kaspi (2020) and Lachmy (2022), when the midtropospheric midlatitude diabatic heating balances a significant portion of the adiabatic cooling by the Ferrel cell ascending branch, condition 1 is not satisfied and the eddy heat flux and eddy-driven jet are latitudinally separated, with the Ferrel cell and eddy-driven jet shifted equatorward relative to the eddy heat flux maximum.

Here, we will use the theoretical framework of Lachmy and Kaspi (2020) to examine the role of midlatitude diabatic heating in the latitudinal jet shift in response to climate change and its relation to the shift of the eddy heat flux. We use an idealized GCM to examine the response of midlatitude diabatic heating to warming over a wide range of climates, forced by either increased CO_2 concentration or increased saturation vapor pressure. We examine whether an opposite shift of the eddy-driven jet and eddy heat flux in response to climate change can be explained based on the role of midlatitude diabatic heating in the zonal-mean heat budget. We consider only the midtropospheric heat budget, focusing on the pressure levels where the Ferrel cell ascent and descent are concentrated. Boundary layer and upper-tropospheric heating terms are left out of the discussion, since they have little effect on the Ferrel cell latitudinal structure. Before presenting the idealized model simulations, we present an analysis of CMIP6 data in order to demonstrate the relation between midlatitude diabatic heating and the intermodel spread of the jet latitude.

The sensitivity of the eddy-driven jet shift to model resolution is examined. We find that the direction of the eddy-driven jet shift in response to climate change is sensitive to the model resolution, with both eddy momentum fluxes and latent heating responding differently to climate change depending on the resolution. Biases in the midlatitude circulation due to coarse resolution have been examined in many previous studies. Several studies found an equatorward jet bias in the coarser-resolution models (e.g., Pope and Stratton 2002; Gerber et al. 2008; Guemas and Codron 2011; Lu et al. 2015). Studies which examined the hydrological circulation found that the precipitation due to parameterized convection decreases with increasing resolution, while the precipitation due to resolved moisture increases (e.g., Herrington and Reed 2017; Lin et al. 2023). Our purpose here is not to investigate the effect of increased resolution on the model performance but rather to connect the midlatitude circulation response to climate change to the diabatic heating response, using the two resolutions as test cases.

The paper is organized as follows. Section 2 describes the CMIP6 data and the idealized aquaplanet model used in this study. Section 3 reviews the equations that we use for analyzing the model output. The CMIP6 data analysis is presented in section 4, and the results from the idealized aquaplanet model simulations are presented in section 5. The conclusions and discussion are given in section 6.

2. Model and data description

In this study, an analysis of CMIP6 data is presented in order to examine the dependence of the jet latitude on the surface temperature and to demonstrate its connection to the

eddy heat flux latitude and to the strength of midlatitude diabatic heating. The CMIP6 data analysis raises theoretical questions regarding the connection between the responses of the jet and the heat budget terms to climate change. To address these questions, we use an idealized aquaplanet model without continents, ice, or clouds, where dynamical mechanisms can be more easily isolated.

a. Analysis of CMIP6 model data

The analysis presented here is limited to the 13 CMIP6 models which output the diabatic heating terms explicitly (Lachmy 2022). The list of models is given in Table 1. We compare between the statistically steady-state periods (50-yr periods; see Lachmy 2022) of the preindustrial and abrupt $4\times CO_2$ simulations, focusing on the Southern Hemisphere (SH) summer. The details of the heat budget and midlatitude circulation are examined for two of the models: INM-CM4-8 and MIROC-ES2L, which exhibit the weakest and strongest midlatitude diabatic heating, respectively. The dependence of the latitude of several midlatitude circulation features on the mean surface temperature in the midlatitudes is examined.

The calculation of the circulation metrics in the CMIP6 models is performed as follows. The latitudes of maximum eddy heat flux and diabatic heating in the midlatitude midtroposphere are calculated after averaging the respective variables over the 410–690-hPa pressure levels. The diabatic heating strength is averaged over the same pressure range (410–690 hPa) and a range of 5° latitude on each side of the diabatic heating maximum. The pressure levels for averaging the diabatic heating and the eddy heat flux were chosen in order to capture their role in the midtropospheric heat budget, which is connected to the Ferrel cell streamfunction. The eddy-driven jet latitude is calculated as the latitude of maximum zonal-mean zonal wind at the pressure level of 860 hPa. This choice is aimed at capturing the latitude of maximum surface westerlies, while avoiding the pressure levels that are partly below the surface. Before calculating the latitudes of maxima, each variable is interpolated at a 0.1° interval using spline interpolation. The vertical level of maximum diabatic heating is calculated within the range of 410–790 hPa, in order to capture its location in all the models. The midlatitude mean surface temperature (MidLatMST) is calculated by averaging the temperature over latitudes 40°–60°S at the surface. The results of this analysis are presented in section 4.

b. Idealized model simulations

The idealized aquaplanet model used in this study is the Model of an Idealized Moist Atmosphere (MiMA; Jucker and Gerber 2017), which is based on the GFDL dynamical core and a previous aquaplanet model (Frierson et al. 2006), with several modifications. MiMA is considered to be an intermediate-complexity model, since it includes more sophisticated diabatic processes than dry dynamical core models, yet it is simplified compared to comprehensive climate models (Maher et al. 2019). The model includes interactive water vapor with latent heat release modeled by a large-scale condensation scheme, Betts–Miller convection (Betts 1986; Betts and Miller

TABLE 1. Specifications of CMIP6 models considered in this study. The models marked in boldface are those for which the spatial distribution of the heat budget terms is shown in Fig. 1.

Modeling protocol	Model	Experiment
CMIP6	CESM2	Preindustrial and abrupt $4\times CO_2$
	CESM2-FV2	
	CESM2-WACCM	
	CESM2-WACCM-FV2	
	CNRM-CM6-1	
	CNRM-ESM2-1	
	GFDL-CM4	
	INM-CM4-8	
	INM-CM5-0	
	IPSL-CM5A2-INCA	
	IPSL-CM6A-LR	
	MIROC-ES2L	
	MIROC6	

1986) with the simplified version described in Frierson (2007). Additionally, the model uses a mixed layer ocean, a Monin–Obukhov boundary layer scheme, and a rapid radiative transfer model (RRTM) radiation scheme (Iacono et al. 2000). The radiation scheme includes the radiative effects of CO_2, ozone, and water vapor, while only the latter is a prognostic variable of the model.

More details of the model can be found in Frierson et al. (2006) (regarding the dynamical core, boundary conditions, surface fluxes, boundary layer, and large-scale condensation parameterizations), Frierson (2007) (regarding the convective parameterization), and Jucker and Gerber (2017) (regarding the radiative parameterization). An example for the applications of this model can be found in Garfinkel et al. (2020). We chose to use this model since moist processes are essential for capturing the effect of diabatic heating in midlatitudes and since the full radiative scheme in this model produces a more realistic circulation than the gray radiation scheme used in the previous aquaplanet model of Frierson et al. (2006), as shown in Tan et al. (2019).

The results presented in this study show sensitivity to the convective heating term in the heat equation; therefore, we dedicate special attention to the convective parameterization. The Betts–Miller convection scheme relaxes the temperature and humidity to specified equilibrium profiles. We follow the choice of Frierson (2007) and use the virtual pseudoadiabat for the temperature equilibrium profile and a constant relative humidity of 0.7 for the humidity equilibrium profile. The model is configured to include deep convection, but without shallow convection. To ensure moist enthalpy conservation in the vertical integral, the time scales of the temperature and humidity relaxation are adjusted so that the precipitation rates associated with humidity and temperature tendencies would be equal (the namelist parameter for this option in the model is called "do_simp"; see Frierson 2007). This scheme also ensures water conservation, since the convective precipitation is equal to the vertical integral of the water vapor loss due to convection.

To obtain the simplest possible configuration for capturing the dynamical link between diabatic heating and the midlatitude circulation, we use an aquaplanet system with zonally symmetric boundary conditions, with no clouds, continents, or ice. The model was run in the equinox configuration. This configuration is compared with the SH summer in CMIP6 models. The motivation for these choices is their relative similarity. The SH summer exhibits relatively weak zonal asymmetries, which makes it reasonable to compare with a zonally symmetric model. The model circulation in a summer configuration is very weak compared to the real SH summer circulation; therefore, we choose to use an equinox configuration, which creates a stronger midlatitude circulation.

To examine the changes in the atmospheric circulation due to increased moisture and the response to climate change, two control parameters are systematically varied. One parameter is the humidity factor (HF; 0.8, 0.9, 1.0, 1.1, and 1.2), which multiplies the saturation vapor pressure (SVP) in the Clausius–Clapeyron equation (as in Frierson et al. 2006, see section 3e). A higher HF leads to increased moisture content and increased latent heat release. The second parameter is the CO_2 concentration (300, 400, 500, and 600 ppm). Both of these parameters affect the temperature and the amount of moisture in the atmosphere. When CO_2 levels rise, it leads to increased temperatures resulting in increased atmospheric moisture due to the Clausius–Clapeyron relation. Increased HF directly increases not only the amount of moisture for a given temperature but also the temperature. This is because the water vapor radiative effect is included in the model, which amplifies the greenhouse effect when the air becomes moister. Additionally, increased humidity enhances the atmospheric static stability (Frierson et al. 2006). The range of parameters used leads to a wide range of climates (Table 2).

All the simulations include 50 model levels in the vertical direction. The model simulations are repeated using two horizontal resolutions (T42 and T85), in order to examine the sensitivity of the results to model resolution. Model simulations are carried out for a 70-yr period. The results are averaged over the statistically steady-state period of the last 20 years of each simulation. The first 50-yr period is considered as spinup, since the warmest simulations take almost 50 years to reach a steady state. Excluding the parameters for representing land and other zonal asymmetries, model parameters are as in Jucker and Gerber (2017) unless specified otherwise. We use a constant albedo of 0.26 in order to obtain relatively realistic surface temperatures.

c. Analysis of the idealized model simulations

The calculation of the circulation metrics in the idealized model, which are presented in section 5, is performed as follows. The latitudes of maximum eddy heat flux, diabatic heating, and Ferrel cell streamfunction are calculated after vertically averaging over the 400–800-hPa pressure levels. The diabatic heating strength is calculated by averaging over the same pressure levels (400–800 hPa) and a range of 5° around the latitude of diabatic heating maximum. This range of levels

TABLE 2. Experimental setup using the idealized GCM MiMA. The control parameters are the HF and the CO_2 concentration. GMST and SVP are the global mean surface temperature and global mean surface saturation vapor pressure, respectively, averaged over the statistically steady-state period. The model resolutions are denoted by the truncation wavenumbers: T42 and T85.

HF	CO_2 concentration (ppm)	T42 GMST (K)	T42 SVP (hPa)	T85 GMST (K)	T85 SVP (hPa)
0.8	300	286.28	12.14	285.57	11.58
	400	287.37	13.04	286.62	12.41
	500	288.25	13.81	287.46	13.11
	600	288.99	14.5	288.18	13.75
0.9	300	287.94	15.23	287.08	14.39
	400	289.12	16.44	288.19	15.48
	500	290.08	17.5	289.11	16.43
	600	290.91	18.45	289.9	17.29
1.0	300	289.81	19.1	288.71	17.79
	400	291.12	20.78	289.95	19.27
	500	292.23	22.31	290.98	20.59
	600	293.23	23.75	291.89	21.82
1.1	300	292.08	24.3	290.63	22.15
	400	293.75	27	292.13	24.37
	500	295.3	29.74	293.37	26.36
	600	296.79	32.61	294.47	28.23
1.2	300	295.57	32.99	293.09	28.25
	400	298.4	39.25	295.07	31.98
	500	301.41	47.08	296.99	36
	600	306.77	64.44	299.02	40.75

is chosen to capture the role of the heating terms in the midtropospheric heat budget. It is slightly different from the midtropospheric pressure level range we used for the CMIP6 data analysis because we use the pressure levels for which the data are available. In both cases, the range used is around the level of maximum Ferrel cell streamfunction, where the structure of the heating terms can be connected to the Ferrel cell structure using the theoretical framework of Lachmy and Kaspi (2020) (see section 1).

The vertical level of maximum diabatic heating and the vertical level where diabatic heating changes sign from positive to negative as the pressure decreases are calculated after latitudinally averaging the diabatic heating over 35°–55°N. The eddy-driven jet latitude is calculated using the zonal-mean zonal wind at 950 hPa. This level was chosen to capture the maximum surface westerlies, but the latitude of maximum zonal wind is not very sensitive to the choice of level within the lower troposphere. For the calculation of the latitudes of maxima, the respective variables are interpolated at the 0.1° interval to get a finer grid, as we considered in the CMIP6 data analysis.

3. Diagnostics

In this section, we review the diagnostic equations that we use for analyzing the output from the CMIP6 models and from the idealized aquaplanet model.

a. Heat budget calculation

The zonal-mean atmospheric heat budget is calculated as a function of pressure and latitude using [e.g., Holton 2004, Eq. (3.6)]

$$\frac{\partial \overline{T}}{\partial t} = -\frac{\overline{v}}{a}\frac{\partial \overline{T}}{\partial \phi} - \overline{\omega}\left(\frac{\partial \overline{T}}{\partial p} - \kappa\frac{\overline{T}}{p}\right) - \frac{1}{a\cos\phi}\frac{\partial[\cos\phi(\overline{v'T'})]}{\partial \phi}$$
$$- \left[\frac{\partial(\overline{\omega'T'})}{\partial p} - \kappa\frac{\overline{\omega'T'}}{p}\right] + \frac{\overline{J}}{c_p}, \quad (1)$$

where T, v, and ω are the temperature, meridional wind, and vertical wind in the pressure coordinates, respectively; p is the pressure; ϕ is the latitude; J is the total diabatic energy tendency; c_p is the specific heat capacity of dry air at constant pressure; R_d is the gas constant of dry air and κ equals R_d/c_p; and a is Earth's radius. An overbar denotes the zonal averaging, and a prime denotes the deviation from the zonal average.

In Eq. (1), the first term on the right-hand side, $-(\overline{v}/a)(\partial\overline{T}/\partial\phi)$, is the *meridional temperature advection by the mean flow*, the second term, $-\overline{\omega}[(\partial\overline{T}/\partial p) - \kappa(\overline{T}/p)]$, is the adiabatic term associated with the zonal-mean vertical motion (hereafter *Ferrel cell heating rate*), the third term, $-[1/(a\cos\phi)]\{\partial[\cos\phi(\overline{v'T'})]/\partial\phi\}$, is the *meridional eddy heat flux convergence*, the fourth term, $-\{[\partial(\overline{\omega'T'})/\partial p] - \kappa(\overline{\omega'T'}/p)\}$, is the *vertical eddy heat flux heating rate*, and the fifth term, $\overline{J}/c_p$, is the *diabatic heating rate* due to convection, condensation, diffusion, and radiation.

The observational study of Lachmy and Kaspi (2020) found that the meridional temperature advection by the mean flow (first term) is negligible and the rest of the terms close the time-mean zonal-mean atmospheric heat budget:

$$-\overline{\omega}\left(\frac{\partial \overline{T}}{\partial p} - \kappa\frac{\overline{T}}{p}\right) - \frac{1}{a\cos\phi}\frac{\partial[\cos\phi(\overline{v'T'})]}{\partial \phi}$$
$$- \left[\frac{\partial(\overline{\omega'T'})}{\partial p} - \kappa\frac{\overline{\omega'T'}}{p}\right] + \frac{\overline{J}}{c_p} \approx 0. \quad (2)$$

In the CMIP6 data analysis presented in section 4, we use the term "*eddy heat flux heating rate*" to refer to the sum of the meridional eddy heat flux convergence (second term on the left-hand side of Eq. (2), $-[1/(a\cos\phi)]\{\partial[\cos\phi(\overline{v'T'})]/\partial\phi\}$) and the vertical eddy heat flux heating rate (third term on the left-hand side of Eq. (2), $-\{[\partial(\overline{\omega'T'})/\partial p] - \kappa(\overline{\omega'T'}/p)\}$). The eddy heat flux heating rate is calculated by subtracting the Ferrel cell heating rate from the temperature tendency due to advection (as in Lachmy 2022). The diabatic heating rate is defined as the "temperature tendency from model physics" in the CMIP6 data output, which consists of the heating due to radiation, large-scale condensation, convection, and boundary layer processes.

b. Mass streamfunction calculation

The zonal-mean meridional mass streamfunction Ψ is derived using

$$\Psi(\phi, p) = \frac{2\pi a\cos\phi}{g}\int_0^p \overline{v}\,dp', \quad (3)$$

where g is the gravitational acceleration of Earth.

c. Moisture budget calculation

The zonal-mean atmospheric moisture budget equation is

$$\frac{\partial \overline{q}}{\partial t} = -\frac{\overline{v}}{a}\frac{\partial \overline{q}}{\partial \phi} - \overline{\omega}\frac{\partial \overline{q}}{\partial p} - \frac{1}{a\cos\phi}\frac{\partial[\cos\phi(\overline{v'q'})]}{\partial \phi} - \frac{\partial(\overline{\omega'q'})}{\partial p} + \overline{S}, \quad (4)$$

where q is the specific humidity (also referred to as moisture) and S is the net source of specific humidity from condensation, convection, and diffusion. In Eq. (4), the first term on the right-hand side, $-(\overline{v}/a)(\partial\overline{q}/\partial\phi)$, is the meridional moisture advection by the mean flow, the second term, $-\overline{\omega}(\partial\overline{q}/\partial p)$, is the vertical moisture advection by the mean flow, the third term, $-[1/(a\cos\phi)]\{\partial[\cos\phi(\overline{v'q'})]/\partial\phi\}$, is the meridional eddy moisture flux convergence, and the fourth term, $-\partial(\overline{\omega'q'})/\partial p$, is the vertical eddy moisture flux convergence.

The *specific humidity tendency due to advection* is calculated as the sum of the four first terms on the right-hand side of Eq. (4). In a statistically steady state, the left-hand side of (4) is near zero and the specific humidity tendency due to advection is equal to minus the *net source term* ($-\overline{S}$). In the idealized model, the net source term represents the sum of the specific humidity tendency from physical parameterizations (large-scale condensation, convection, and diffusion). In our model data analysis, the moisture budget terms are multiplied by L_v/c_p to express them in temperature tendency units.

d. Momentum budget calculation

The zonal-mean atmospheric momentum budget equation is

$$\frac{\partial \overline{u}}{\partial t} = f\overline{v} - \frac{\overline{v}}{a}\frac{1}{\cos\phi}\frac{\partial[\cos\phi(\overline{u})]}{\partial \phi} - \overline{\omega}\frac{\partial \overline{u}}{\partial p}$$
$$- \frac{1}{a\cos^2\phi}\frac{\partial[\cos^2\phi(\overline{u'v'})]}{\partial \phi} - \frac{\partial(\overline{\omega'u'})}{\partial p} - \overline{F_x}, \quad (5)$$

where u is the zonal wind, f is the Coriolis parameter, and F_x is the friction. In Eq. (5), the first term on the right-hand side, $f\overline{v}$, is the *Coriolis force*, the second term, $-(\overline{v}/a)(1/\cos\phi)\{\partial[\cos\phi(\overline{u})]/\partial\phi\}$, is the *meridional momentum advection by the mean flow*, the third term, $-\overline{\omega}(\partial\overline{u}/\partial p)$, is the *vertical momentum advection by the mean flow*, the fourth term, $-[1/(a\cos^2\phi)]\{\partial[\cos^2\phi(\overline{u'v'})]/\partial\phi\}$, is the *meridional eddy momentum flux convergence*, and the fifth term, $-[\partial(\overline{\omega'u'})/\partial p]$, is the *vertical eddy momentum flux convergence*.

e. Clausius–Clapeyron equation

The Clausius–Clapeyron equation is used for calculating the saturation vapor pressure in the aquaplanet model, given the temperature and assuming fixed latent heat of vaporization [Frierson et al. 2006, Eq. (22)]:

$$P(T) = P(T_0)\exp\left[-\left(\frac{L_v}{R_v}\right)\left(\frac{1}{T} - \frac{1}{T_0}\right)\right], \quad (6)$$

where $P(T)$ is the saturation vapor pressure at temperature T, $T_0 = 273.16$ K is a constant reference temperature, R_v is the

gas constant for water vapor, and L_v is the latent heat of evaporation.

In the idealized aquaplanet model, the reference saturation vapor pressure $P(T_0)$ is multiplied by a nondimensional parameter, which we call "the humidity factor" (see section 2b). HF controls the humidity content in the atmosphere through the saturation vapor pressure (as in Frierson et al. 2006). To calculate the saturation vapor pressure in the model, we multiplied HF by the vapor pressure calculated using Eq. (6), where $L_v = 2.5 \times 10^6$ J kg^{-1}, $R_v = 461.5$ J kg^{-1} K^{-1}, and $P(T_0) = 610.78$ Pa.

4. Midlatitude atmospheric circulation in CMIP6 models

a. The heat budget and its response to climate change

The latitude of the eddy-driven jet shows a large intermodel variability in CMIP6 models, though this variability is reduced compared to CMIP5 (Curtis et al. 2020). Lachmy (2022) found a negative correlation between the midlatitude diabatic heating strength and the eddy-driven jet latitude during SH summer in the intermodel variability in CMIP6 models. Here, we examine the climatological heat budget in two extreme cases: one model with strong midlatitude diabatic heating and a more equatorward eddy-driven jet (MIROC-ES2L) and another model with weak diabatic heating and a more poleward eddy-driven jet (INM-CM4-8). The heat budget terms, mass streamfunction, and zonal-mean zonal wind in these two models (marked in boldface in Table 1) are shown in Fig. 1. The heat budget terms presented in Fig. 1 are defined in section 3a.

To keep the analysis relatively simple, only the SH summer [December–February (DJF)] is considered. The colored shading in Fig. 1 represents the preindustrial climate and the colored contours represent the response to climate change defined as the difference between the abrupt $4\times CO_2$ experiment and the preindustrial experiment. The gray solid and dashed lines in Fig. 1 represent the mass streamfunction of the atmospheric circulation in the preindustrial experiment.

There are notable differences in the structure of the midlatitude circulation between the two models, which can be understood in terms of the zonal-mean heat and momentum budgets. The Ferrel cell mass streamfunction is relatively weak and wide in INM-CM4-8 compared to MIROC-ES2L. The polar cell is confined to the polar region in INM-CM4-8, while in MIROC-ES2L, it is quite established at 60°S. Consistent with the differences in the structure of the mass streamfunction, the region of the strongest negative Ferrel cell heating rate in the midtroposphere is more poleward in INM-CM4-8 (around latitude 60°S), where it is balanced mostly by the eddy heat flux heating rate [Figs. 1a(1),b(1),c(1)], while in MIROC-ES2L, it is located more equatorward (around latitude 50°S), and it is mostly balanced by diabatic heating [Figs. 1a(2),b(2),c(2), note the positive maximum of diabatic heating around 600 hPa and 50°S and the strong negative values of the Ferrel cell heating rate around the same location, while the eddy heat flux heating rate there is nearly zero]. The jet stream is located inside the Ferrel cell in both models [Figs. 1d(1),d(2)]. The jet is more equatorward in the MIROC-

ES2L model, consistent with the more equatorward Ferrel cell maximum streamfunction.

The conditions for the collocation of the eddy heat flux and eddy-driven jet suggested by Lachmy and Kaspi (2020) (see section 1) can be used to interpret the circulation differences between these two models. The latitudes of maximum eddy heat flux and Ferrel cell streamfunction in the midtroposphere are closer in the INM-CM4-8 model compared to the MIROC-ES2L model. This can be seen by comparing the maximum streamfunction and the latitude of zero eddy heat flux heating rate around 600 hPa in Figs. 1b(1) and 1b(2) (in the INM-CM4-8 model, the maximum eddy heat flux latitude is 47.9°S and the maximum Ferrel cell streamfunction latitude is 48.2°S in the preindustrial experiment, whereas in the MIROC-ES2L model, these latitudes are at 49.8° and 43.1°S, respectively). This means that condition 1 is approximately satisfied in INM-CM4-8, but not in MIROC-ES2L. The eddy-driven jet is located inside the Ferrel cell (in both models, consistent with conditions 2 and 3) and is thus closer to the maximum eddy heat flux in the INM-CM4-8 model compared to the MIROC-ES2L model.

A strong positive correlation between midlatitude diabatic heating and the latitudinal separation between the eddy heat flux and eddy-driven jet in CMIP6 models was found in Lachmy (2022). The comparison between the heat budgets of the two models demonstrates that this correlation can be explained by the conditions suggested in Lachmy and Kaspi (2020). As shown in Lachmy (2022), the eddy heat flux peak latitude is almost constant across various models, when considered separately for each of the experiments (preindustrial and abrupt $4\times CO_2$). Consequently, a higher latitudinal separation between the eddy heat flux and the eddy-driven jet is associated with a more equatorward eddy-driven jet. This explains the negative correlation between diabatic heating and the eddy-driven jet latitude found in Lachmy (2022).

In terms of the response to climate change, a poleward and upward shift is noticed in the Ferrel cell heating rate, the heating rate due to total eddy heat flux, diabatic heating, and the jet stream in both models, with a more notable poleward shift in the MIROC-ES2L model. Note that the MIROC-ES2L model has a more equatorward eddy-driven jet latitude in the preindustrial simulation and a stronger poleward shift in response to climate change, compared with INM-CM4-8. This is consistent with previous studies, which found a negative correlation between the preindustrial jet latitude and the poleward jet shift in response to climate change (Kidston and Gerber 2010; Simpson and Polvani 2016; Curtis et al. 2020; Simpson et al. 2021).

b. Latitudinal shifts as a function of surface temperature

Previous studies explained the poleward shift of the eddy heat flux and eddy-driven jet in response to climate change based on the poleward shift of the baroclinically unstable zone with increased surface temperature due to increased static stability on the equatorward side of the baroclinic zone (e.g., Frierson 2008; Lu et al. 2010; Butler et al. 2011). Following this reasoning, we would expect the maximum eddy heat
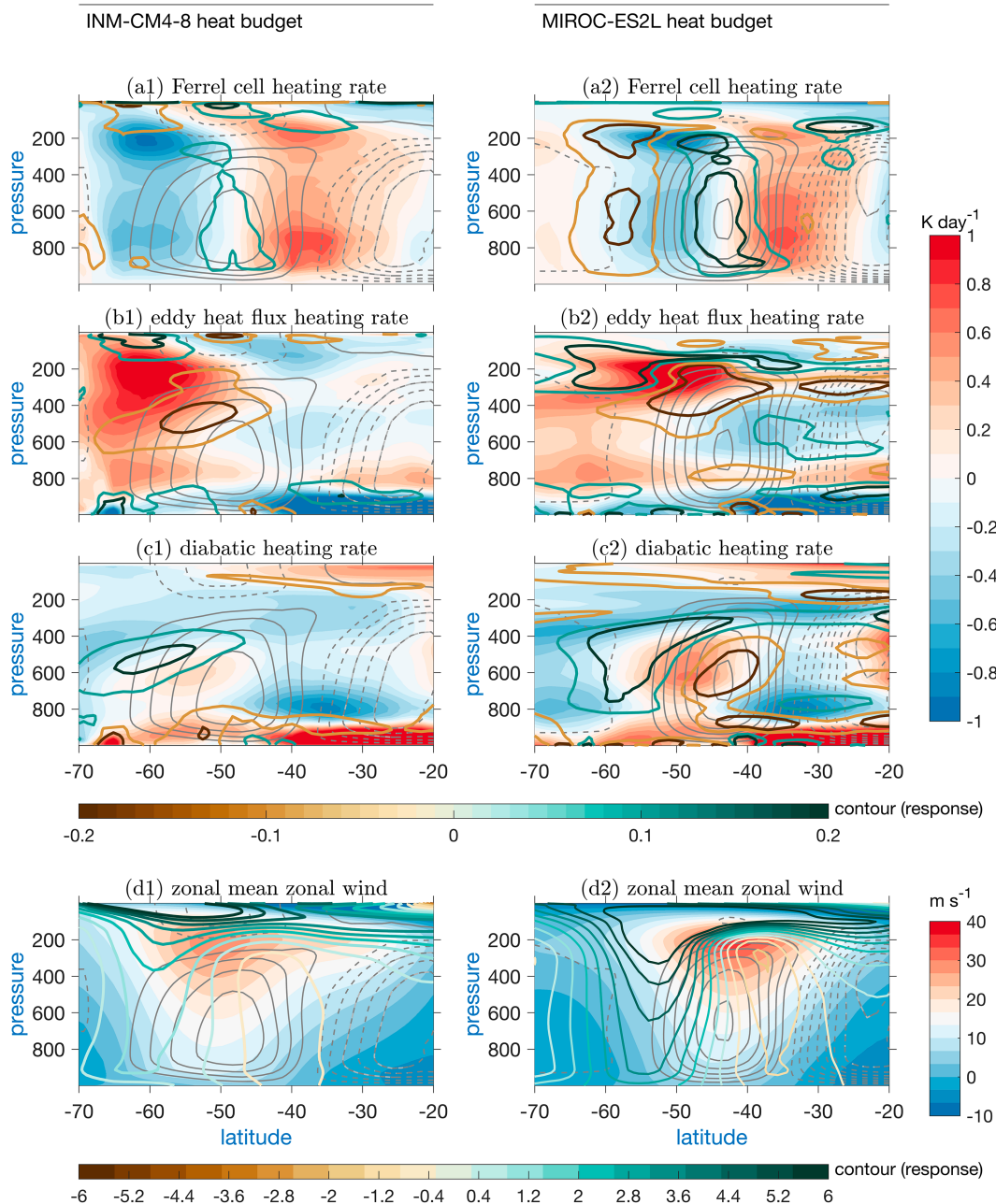
FIG. 1. Heat budget terms and the zonal-mean zonal wind in the SH summer (DJF) in the preindustrial experiment (shaded colors) and the response to quadrupled CO_2 concentration (colored contours) for two different CMIP6 models: INM-CM4-8 and MIROC-ES2L. The heating terms include (a1),(a2) Ferrel cell heating rate (K day^{-1}), (b1),(b2) eddy heat flux heating rate (K day^{-1}), (c1),(c2) diabatic heating rate (K day^{-1}), and (d1),(d2) the zonal-mean zonal wind (m s^{-1}). Solid and dashed gray contours represent the positive and negative values of the mass streamfunction in the preindustrial experiment, respectively, with a contour interval of 5×10^9 kg s^{-1}. The zero contour is omitted.

flux to be located more poleward in models with a higher surface temperature. The latitude of the eddy-driven jet would follow the latitude of the maximum eddy heat flux to the extent that conditions 1–3 from Lachmy and Kaspi (2020) are satisfied. However, the relation between the latitudes of the eddy heat flux and eddy-driven jet could be modified due to

the intermodel spread in midlatitude diabatic heating, as suggested in Lachmy (2022) and demonstrated in the previous subsection. This is because in models with a strong midlatitude, diabatic heating condition 1 is not satisfied. Here, we examine how the intermodel spread in surface temperature in the midlatitudes is related to the spread in the eddy-driven jet latitude.
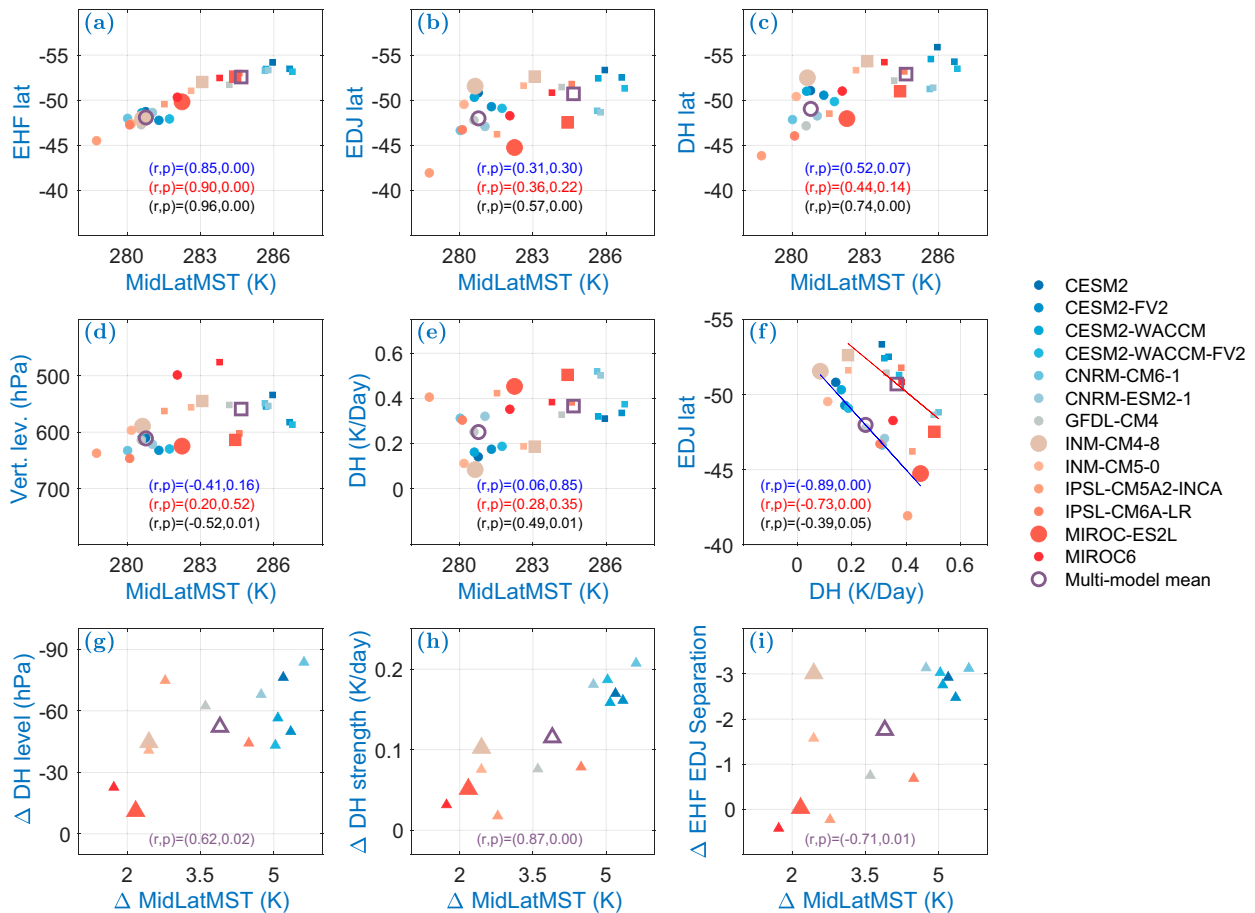
FIG. 2. (top) Latitudes of maxima of the following variables in CMIP6 models (Table 1) for the SH summer vs mean midlatitude surface temperature (MidLatMST): (a) eddy heat flux (EHF), (b) eddy-driven jet (EDJ), and (c) midlatitude diabatic heating (DH). (middle) Shown are (d) vertical level of maximum DH vs MidLatMST, (e) DH strength vs MidLatMST, and (f) EDJ latitude vs DH strength. (bottom) The response (denoted by Δ) of the following variables to climate change vs the MidLatMST response: (g) DH level, (h) DH strength, and (i) the EHF–EDJ latitudinal separation. The circles, squares, and triangles represent the preindustrial experiment, the abrupt 4×CO_2 experiment, and the response, respectively, with the color representing the model. Empty markers represent the multimodel mean. Larger markers represent the models for which the heat budget is presented in Fig. 1. The correlation r between the variables within each panel is written in the bottom of each panel with its p value, where blue, red, black, and purple colors represent the preindustrial, abrupt 4×CO_2, both experiments together, and the response, respectively. For the correlations, we consider the latitude as positive in the SH.

The CMIP6 intermodel variability of the latitudes of maxima eddy heat flux, eddy-driven jet and diabatic heating, and the vertical level of maximum diabatic heating along with the strength of diabatic heating are plotted as a function of the mean midlatitude surface temperature in Fig. 2, for the preindustrial (marked by circles) and abrupt 4×CO_2 (marked by squares) experiments (see section 2a for the analysis methods). A poleward shift of the eddy heat flux, eddy-driven jet, and diabatic heating can be observed in response to climate change (Figs. 2a–c). The midlatitude surface temperature changes widely between models. In all the models, the temperature increases in response to quadrupled CO_2, but the intermodel differences in surface temperature are of the same order of magnitude as the response to quadrupled CO_2.

It can be seen that the poleward shift of the eddy heat flux latitude is quite monotonic as a function of temperature, with

a high correlation (0.85 in the preindustrial experiment, 0.90 in the abrupt 4×CO_2 experiment, and 0.96 for the two experiments together, Fig. 2a). This relation is consistent with theoretical arguments put forward in previous studies (e.g., Lu et al. 2010; Shaw 2019). A positive correlation can be observed between the mean midlatitude surface temperature and the latitudes of the eddy-driven jet (0.31, 0.36, and 0.57 in the preindustrial, abrupt 4×CO_2, and two experiments together, respectively; Fig. 2b) and diabatic heating (0.52, 0.44, and 0.74 in the preindustrial, abrupt 4×CO_2, and two experiments together, respectively; Fig. 2c), but these correlations are weaker and less significant than the correlation between the midlatitude surface temperature and the eddy heat flux latitude.

As explained above, increased midlatitude midtropospheric diabatic heating is associated with a larger separation between the eddy heat flux and eddy-driven jet. The larger separation

between the eddy heat flux and eddy-driven jet in models with stronger diabatic heating is mostly expressed by a more equatorward eddy-driven jet, while the differences in the eddy heat flux latitude between the models are more subtle (Figs. 4d–f of Lachmy 2022). The negative correlation between the eddy-driven jet latitude and midlatitude diabatic heating for each of the experiments separately is shown in Fig. 2f, similar to the result shown in Lachmy (2022).

Midlatitude diabatic heating depends on the circulation and on temperature. In terms of temperature dependence, latent heating, which is the dominant component of diabatic heating in the midlatitudes, is expected to intensify in a warmer climate. This is due to an increase in moisture content following the Clausius–Clapeyron relation. Additionally, as surface temperatures rise, condensation is expected to occur at higher altitudes, leading to higher-level latent heating. The level of maximum midlatitude diabatic heating and its strength increase with climate change, but are not significantly correlated with temperature in the intermodel spread of each individual experiment (Figs. 2d,e). The reason for this lack of significant correlation between midlatitude diabatic heating and temperature is beyond the scope of this work. We point to the possibility that different convective parameterizations in different models could contribute to the large intermodel spread in diabatic heating, as these parameterizations were shown to contribute to the spread in the lapse rate and jet latitude by Fuchs et al. (2023).

These results suggest that the responses of midlatitude diabatic heating and eddy heat flux to increased temperatures may have opposite effects on the eddy-driven jet latitude. On the one hand, increased surface temperature causes a poleward shift of the eddy heat flux, which could be associated with a poleward shift of the eddy-driven jet. On the other hand, increased midlatitude midtropospheric diabatic heating could be associated with a more equatorward eddy-driven jet latitude (Fig. 2f here and Figs. 4 and 5 in Lachmy 2022). The effect of diabatic heating could, at least partly, explain the lower correlation of the eddy-driven jet latitude with temperature, compared to that of the eddy heat flux latitude (Figs. 2a,b).

We further investigate the spread in the response to climate change. Figures 2g–i show the relation between the responses of the maximum diabatic heating level, diabatic heating strength, the latitudinal separation between the eddy heat flux and eddy-driven jet, and the response of midlatitude mean surface temperature. The responses, denoted by Δ, are calculated as the values in the abrupt $4\times CO_2$ experiment minus the preindustrial. Models with a stronger temperature response generally show a stronger upward shift of the diabatic heating (with a 0.62 correlation, Fig. 2g) and a more pronounced strengthening of the diabatic heating (with a 0.87 correlation, Fig. 2h). Additionally, a stronger temperature response is correlated with a larger latitudinal separation response between the eddy heat flux and eddy-driven jet latitude (with a 0.71 correlation, Fig. 2i). We argue that the relation between the temperature response and the diabatic heating response explains the relation between the temperature response and the response of the latitudinal separation between the eddy heat flux and eddy-driven jet. This argument is supported by the high correlation (0.93) found by

Lachmy (2022) between the diabatic heating strengthening and the increase in latitudinal separation in CMIP6 models (Fig. 5d of Lachmy 2022).

Overall, these results imply a potential role of diabatic heating in the intermodel spread of the eddy-driven jet latitude and its response to climate change. To study this connection systematically, we use a series of idealized model simulations, presented in the following section.

5. The midlatitude atmospheric circulation response to climate change in an idealized GCM

The analysis of the CMIP6 output presented in the previous section suggests that the response of midlatitude diabatic heating to temperature changes is connected to variations in the eddy-driven jet latitude. However, the dynamics underlying this connection are difficult to determine using CMIP6 output data due to the complexity of the models, the limited range of simulated climates for which the relevant data are available, and the relatively low spatial and temporal resolution of the available data. For these reasons, we use the idealized aquaplanet GCM described in section 2b to systematically examine the responses of midlatitude diabatic heating and the midlatitude circulation to warming and the connection between these responses. The model setup and the series of experiments are described in section 2b and summarized in Table 2.

a. Latitudinal shifts of the midlatitude atmospheric circulation in response to warming

The latitudes of various metrics in the model simulations are presented in Fig. 3 as a function of the global mean surface temperature (GMST) and SVP. It is important to note that the SVP is a function of the GMST and the humidity factor, as calculated from Eq. (6) and multiplied by the humidity factor (see section 2b). SVP is the main variable that determines the climate, rather than the GMST itself. This can be observed in Fig. 3, where each SVP value corresponds to a single metric value, whereas a given GMST corresponds to multiple metric values depending on the humidity factor [e.g., in Fig. 3b(3), the simulations labeled "600CO2-hf1.0" and "400CO2-hf1.1" have different eddy-driven jet latitudes, but a similar GMST, while in Fig. 3b(4), they are shown to have different SVP values]. Replacing the global mean surface temperature with the midlatitude mean surface temperature yields qualitatively similar results (not shown).

The latitudes shown in Fig. 3 include the maxima of the eddy heat flux, the eddy-driven jet, the Ferrel cell streamfunction, and the midlatitude diabatic heating (see section 2c for the calculation methods). It is found that the eddy heat flux [Figs. 3a(1)–a(4)], eddy-driven jet [Figs. 3b(1)–b(4)], Ferrel cell [Figs. 3c(1)–c(4)], and diabatic heating [Figs. 3d(1)–d(4)] latitudes shift poleward with increased GMST or SVP for low (T42: *first block*) and high (T85: *second block*) resolution simulations (Fig. 3), with the exception of a certain range of climates in the T42 simulations. In the T42 simulations, the eddy heat flux latitude is almost constant between GMST 293 to 296 K (SVP 23–34 hPa) [Figs. 3a(1),a(2)], while the eddy-driven jet [Figs. 3b(1),b(2)], Ferrel cell maximum streamfunction [Figs. 3c(1),c(2)], and maximum midlatitude diabatic heating
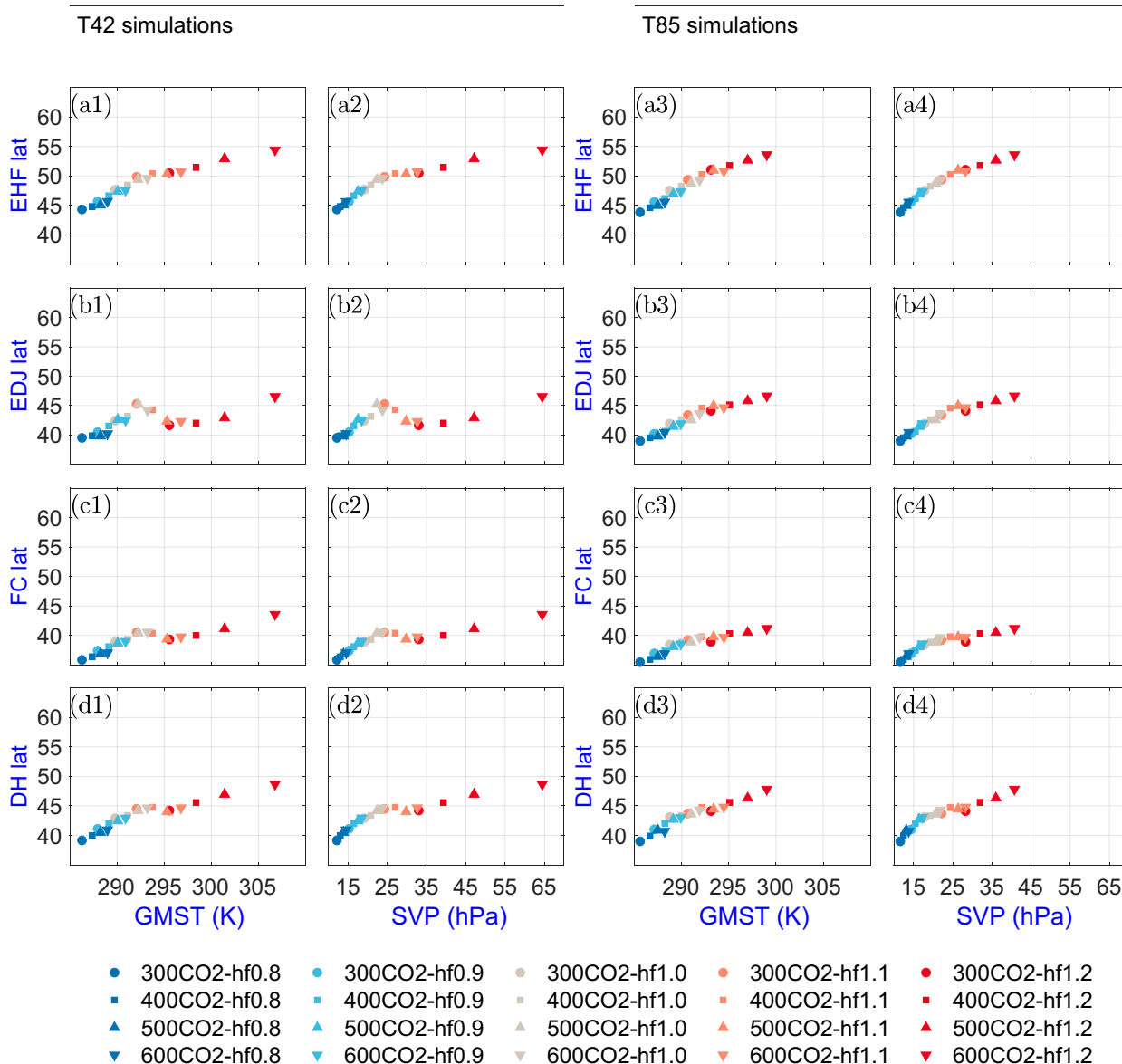
FIG. 3. The latitudes of various midlatitude circulation metrics in the idealized GCM simulations described in section 2b and Table 2, as a function of GMST and SVP. Each marker refers to a different simulation, where the CO_2 concentration (CO_2; ppm) and HF values of each corresponding simulation are shown in the legend. (a1)–(d1),(a2)–(d2) First and (a3)–(d3),(a4)–(d4) second blocks represent the simulations using T42 and T85 resolutions, respectively. (first row) The latitude of the EHF maximum and (second row) the latitude of the EDJ. (third row) The latitude of the maximum of the FC and (fourth row) latitude of the maximum of the midlatitude DH.

[Figs. 3d(1),d(2)] show an equatorward shift in response to warming or increased SVP at this range of climates.

The absence of an equatorward shift of the eddy-driven jet in response to increased SVP in the T85 simulations and the existence of this shift in the T42 simulations for a certain range of climates could imply that numerical effects are playing a role in this phenomenon. However, an equatorward shift of the eddy-driven jet in response to climate change was found in several idealized model studies (Pfahl et al. 2015; Dwyer and O'Gorman 2017; Lachmy and Shaw 2018; Tan et al. 2019; Davis and Birner 2022), in some cases when using

T85 resolution (Pfahl et al. 2015). The direction of the eddy-driven jet shift was found to depend on radiative (Tan et al. 2019; Davis and Birner 2022) and convective (Garfinkel et al. 2024) parameterizations. Even though model configurations leading to an equatorward jet shift in response to climate change are generally less realistic, this phenomenon is of interest, since it challenges our understanding of the midlatitude circulation response. Some of the proposed theoretical explanations for the poleward jet shift in response to climate change are based on the thermal response, which does not differ substantially between the cases showing opposite jet shifts
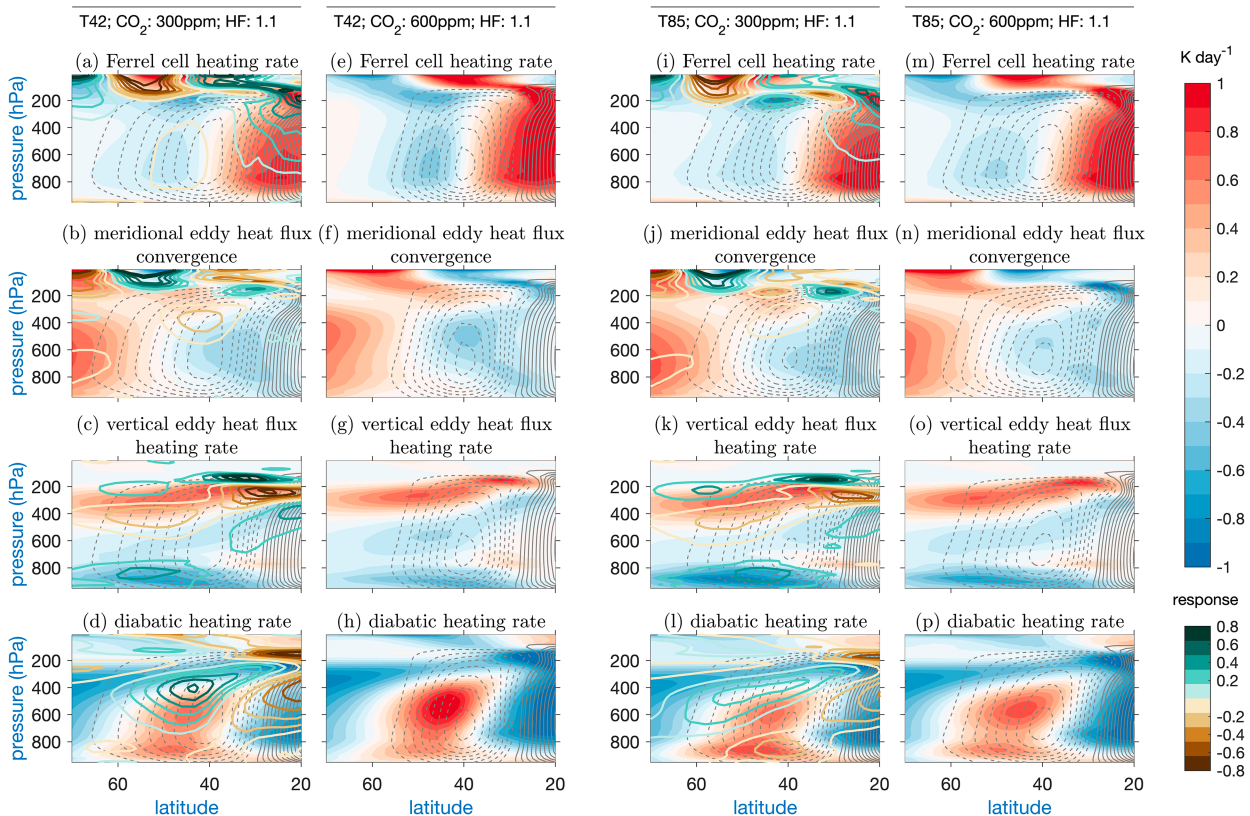
FIG. 4. Heat budget terms (shaded; K day^{-1}) over the midlatitudes in the cooler (CO$_2$: 300 ppm and HF: 1.1) and warmer (CO$_2$: 600 ppm and HF: 1.1) simulations in the idealized GCM, and the difference between the warmer and cooler simulations (colored contours; K day^{-1}). The plotted heat budget terms are (first row) Ferrel cell heating rate, (second row) meridional EHF convergence, (third row) vertical EHF heating rate, and (fourth row) DH rate. The first block represents the simulations using T42 resolution and the second block represents high-resolution simulations using T85. The left and right columns of each block represent the cooler and warmer simulations, respectively. Solid and dashed contours represent the positive and negative values of the mass streamfunction, respectively, with a contour interval of 5×10^9 kg s^{-1}.

(Tan et al. 2019). We argue here that the equatorward eddy-driven jet shift in the T42 simulations is related to the response of midlatitude diabatic heating to climate change, which is different in the T85 simulations. While the differences in the diabatic heating response between the T42 and T85 simulations arise from the different resolutions, these two sets of simulations provide the opportunity to examine how the circulation response is dynamically related to the diabatic heating response. We will examine next the different responses of the circulation to climate change in the T42 and T85 simulations, in the range of SVP that shows opposite shifts of the eddy-driven jet, in order to better understand the conditions that lead to these opposite shifts.

b. Midlatitude heat budget

As discussed previously in the context of the intermodel spread of the eddy-driven jet latitude in CMIP6 models, models with stronger midlatitude midtropospheric diabatic heating have a more equatorward eddy-driven jet (Fig. 2f), which can be explained by the zonal-mean heat budget (Lachmy and Kaspi 2020) (see section 1). Here, we use the same

framework [Eq. (2)] to explain the different shifts of the eddy-driven jet in response to climate change in the T42 and T85 simulations. Each term of the heat budget Eq. (2) is plotted in Fig. 4 for the cooler and warmer climates. We consider the simulation with CO$_2$ concentration 300 ppm and humidity factor of 1.1 as the cooler climate and the simulation with CO$_2$ concentration 600 ppm and the same humidity factor of 1.1 as the warmer climate. We choose this pair of climates since this is approximately the range of climates at which the T42 simulations exhibit an equatorward jet shift with warming, while the T85 simulations do not [see Figs. 3b(1)–b(4)]. The mass streamfunction is calculated using Eq. (3). In all the simulations shown, the heat budget is closed, i.e., the residual in Eq. (2) is negligible (not shown). The qualitative resemblance of the heat budget terms and their response to climate change in the idealized model to those in the CMIP6 models confirms the relevance of this model for capturing the leading order processes controlling the heat budget response to climate change (cf. Fig. 4 with Fig. 1, where the eddy heat flux heating rate represents the sum of the heating by meridional eddy heat flux convergence and vertical eddy heat flux heating rate).

The heat budget terms in the colder and warmer simulations with the two resolutions (Fig. 4) indicate that the equatorward eddy-driven jet shift found in the T42 simulations is related to the response of midlatitude diabatic heating to climate change, which is different from its response in the T85 simulations. In the T42 simulations, it can be seen that while the meridional eddy heat flux convergence shifts upward in response to climate change with not much change in its latitudinal structure (Figs. 4b,f), the changes in the latitudinal structure of the Ferrel cell heating rate and the diabatic heating are significant in response to climate change. The ascending branch of the Ferrel cell becomes narrower and shifts equatorward, leading to stronger cooling by the upward motion around latitudes 45°–50°N (Figs. 4a,e). This stronger cooling is partly balanced by stronger midlatitude midtropospheric diabatic heating (Figs. 4d,h).

This response of the heat budget terms indicates that the equatorward shift of the maximum Ferrel cell streamfunction in response to climate change in the T42 simulations is connected to the strengthening response of midlatitude diabatic heating, through the constraint of the zonal-mean heat balance. These results are consistent with the differences in the heat budget and circulation between the two CMIP6 models examined in Fig. 1, where the model with stronger midlatitude diabatic heating has a narrower ascending branch of the Ferrel cell and its maximum streamfunction is more equatorward. The eddy-driven jet latitude is linked to the maximum Ferrel cell streamfunction latitude through conditions 2 and 3 (see section 1). These conditions are approximately satisfied in the CMIP6 models as well as the idealized model simulations presented here, as evident from the high correlation between the maximum Ferrel cell streamfunction latitude and the eddy-driven jet latitude [Figs. 3b(2),c(2) and Fig. 4c in Lachmy (2022)]. These results link the equatorward shift of the eddy-driven jet to the strengthening of the midlatitude diabatic heating.

In the T85 simulations, there is no significant latitudinal shift of the Ferrel cell streamfunction and the associated heating term in response to climate change for this range of parameters (Figs. 4i,m). Consistent with the argument connecting the equatorward shift of the circulation to the diabatic heating response in the T42 simulations, it can be seen that the diabatic heating response in the T85 simulations is much weaker (Figs. 4d,l and 5c,f in the next subsection). All the circulation components and heating terms, i.e., Ferrel cell heating rate, heating due to meridional and vertical eddy heat flux, and diabatic heating are shifted upward and slightly poleward in response to warming in the T85 simulations.

The appearance of the polar cell can be observed in the warmer simulation with the T42 resolution, while it is much weaker and narrower in the cooler simulations for both resolutions and in the warmer simulation with the T85 resolution (Fig. 4 and Fig. S1 in the online supplemental material). In the T42 simulations with SVP less than 24.3 hPa (experiment with CO_2: 300 ppm and HF: 1.1), the polar cell is nearly absent or very weak (not shown). At this range of parameters, the jet shifts poleward with warming [Fig. 3b(2)]. When the SVP increases above 24.3 hPa, there is a transition to a regime

with a polar cell and the eddy-driven jet shifts equatorward with increased SVP, but the eddy heat flux stays approximately at the same latitude [Figs. 3a(2),b(2)]. For SVP values above 33 hPa, the eddy-driven jet and eddy heat flux both shift poleward with increased SVP [Figs. 3a(2),b(2)], while the polar cell remains (not shown). In the T85 simulations, the polar cell is very weak for all the climates examined here. The equatorward jet shift in the T42 simulations with increased SVP as the polar cell appears is related to the strong diabatic heating, which balances the adiabatic cooling by the Ferrel cell (the cooling at the ascending branch becomes stronger when the polar cell appears), while the meridional eddy heat flux convergence balances the diabatic cooling at high latitudes (Figs. 4e–h).

c. Vertical shift and strengthening of the midlatitude diabatic heating

In the previous subsections, it was shown that an equatorward shift of the Ferrel circulation and the eddy-driven jet in response to climate change occurs in the T42 simulations for a certain range of parameters, while in the rest of the parameter range and in the T85 simulations, the Ferrel cell and the eddy-driven jet shift poleward in response to climate change. It was suggested that the equatorward shift is connected to a strengthening of the midlatitude midtropospheric diabatic heating. We wish to examine next the properties of the midlatitude diabatic heating response to climate change for the full range of parameters, in order to assess how these properties are related to the direction of the jet shift. We examine the vertical shift of midlatitude diabatic heating by measuring the level of maximum midlatitude diabatic heating (Figs. 5a,d) and the level where the midlatitude diabatic heating changes sign from positive to negative as the pressure decreases (Figs. 5b,e), as well as the strength of the diabatic heating averaged over the midlatitude midtroposphere (Figs. 5c,f), as a function of SVP. The calculation methods for these metrics are presented in section 2c.

The dependence of the vertical level of maximum diabatic heating on the SVP is similar in the T42 and T85 simulations. It can be seen that the maximum midlatitude diabatic heating shifts from the boundary layer to the midtroposphere when the SVP increases beyond 24.3 hPa in the T42 simulation (24.4 hPa for the T85 simulation). While this shift seems abrupt in Figs. 5a and 5d, it represents a gradual weakening of the diabatic heating in the boundary layer and strengthening in the midtroposphere. The vertical level where diabatic heating changes sign also depends similarly on SVP in the T42 and T85 simulations (Figs. 5b,e). For both resolutions, this vertical level shifts upward (i.e., to levels with lower pressure) as the SVP increases. Note that the SVP in the T42 simulations reaches higher values for a given set of parameters (CO_2 concentration and humidity factor), compared with the SVP in the T85 simulations with the same parameters. However, the vertical shift of diabatic heating as a function of SVP is quite similar for the two resolutions.

The response of the diabatic heating strength to increased SVP shows a notable difference between the two resolutions,
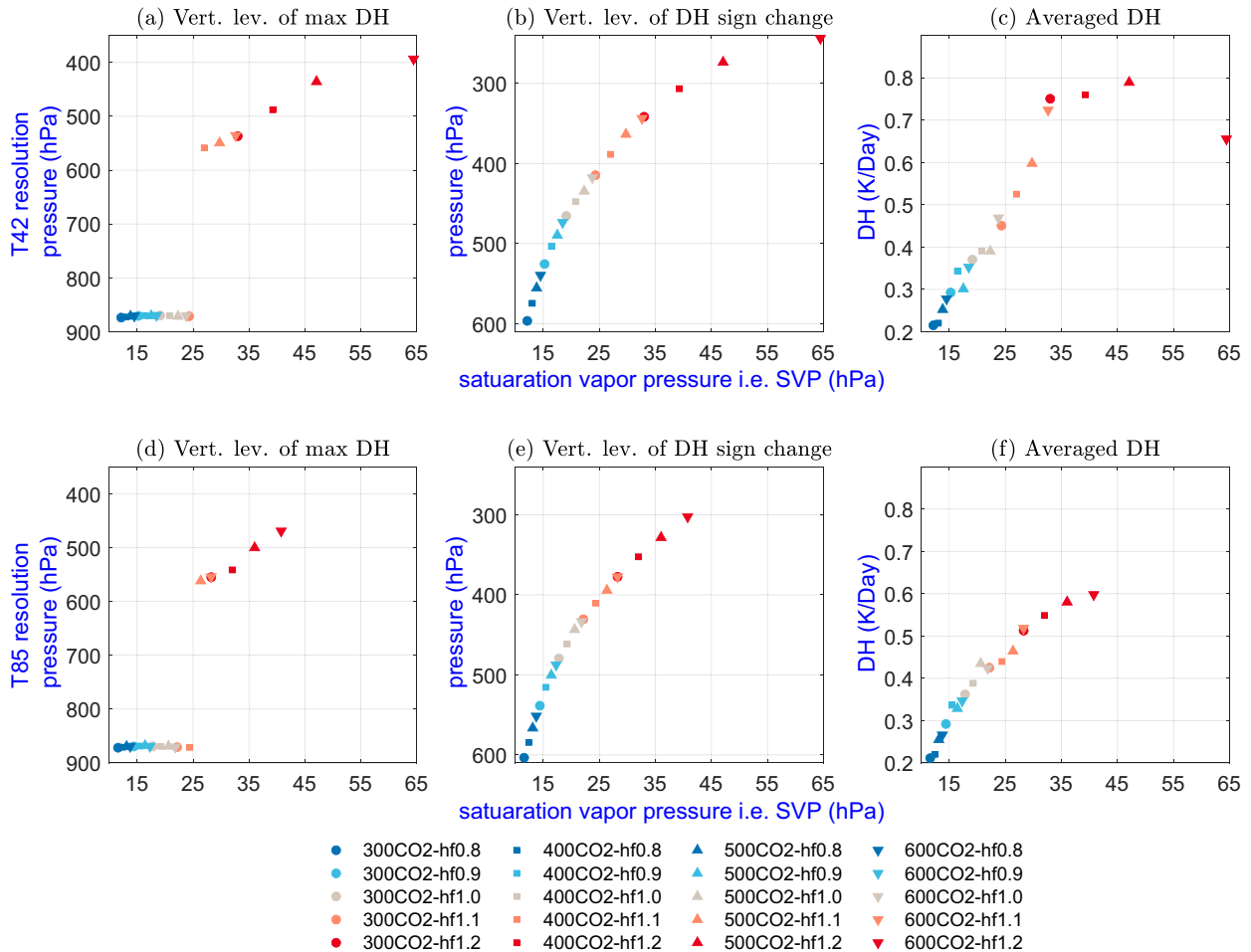
FIG. 5. DH strength and the vertical level of maximum DH in (a)–(c) T42 and (d)–(f) T85 simulations using the idealized GCM showing (left) vertical level of maximum DH, (center) the vertical level of the change in sign of DH, and (right) the averaged DH over the midlatitude midtroposphere (K day^{-1}).

for SVP values beyond 20 hPa (Figs. 5c,f). In the range of SVP between 20 and 35 hPa, diabatic heating increases from around 0.4 to 0.75 K day^{-1} in the T42 simulations and from 0.4 to 0.58 K day^{-1} in the T85 simulations. The opposite shifts of the eddy-driven jet are within this range of SVP values [Figs. 3b(2),b(4)], which supports the assumption that the equatorward shift of the jet in the T42 simulations is related to the strengthening of the midlatitude midtropospheric diabatic heating. At SVP values higher than 35 hPa, the midlatitude diabatic heating becomes concentrated in the upper troposphere (pressure levels of 325 hPa and less, Figs. 5b,e), so that it cannot balance the Ferrel cell cooling in the midtroposphere and the eddy-driven jet continues to shift poleward with the eddy heat flux [Fig. 3b(2)]. Overall, in the T42 simulations, it is noticed that at the transition where the polar cell appears (SVP increases above 24.3 hPa), the diabatic heating is shifted upward and strengthens and becomes dominant in the midtropospheric heat budget. This leads to a decoupling between the eddy heat flux, which stays roughly at the same latitude, and the eddy-driven jet and Ferrel cell, which shift

equatorward. In the rest of the parameter space (lower or higher SVP), the eddy heat flux and eddy-driven jet shift poleward with increased SVP at a similar rate because the role of diabatic heating in the midtroposphere is not significantly changed between these simulations.

d. Midlatitude diabatic heating terms and the moisture budget

The results of the previous subsections indicate that the direction of the eddy-driven jet shift in response to climate change is related to the response of midlatitude diabatic heating. In the range of parameters where the midlatitude midtropospheric diabatic heating does not increase much with warming, the eddy-driven jet shifts poleward with the eddy heat flux. When diabatic heating increases significantly in the midlatitude midtroposphere, the eddy-driven jet shifts equatorward. While this connection is explained based on the constraint of the zonal-mean heat balance and the relation between the Ferrel circulation and the eddy-driven jet, this explanation does not imply a causal relation, as the eddy-

driven jet and diabatic heating can be mutually dependent or can depend both on a third element of the circulation. Specifically, the latent heating component of the diabatic heating is partly due to eddy moisture flux convergence, which depends on the properties of midlatitude eddies, which drive the jet. To investigate this relationship, we break down the diabatic heating into its latent heating and radiative components and compare the total parameterized latent heating with the latent heat release associated with moisture (i.e., specific humidity) tendency.

Midlatitude diabatic heating is decomposed into radiative and latent heating. The radiative heating is the sum of the temperature tendency due to longwave and shortwave radiation. The latent heating is the sum of temperature tendency from large-scale condensation, convection, and diffusion. We use the term "latent heating" for brevity, though heating due to convection and diffusion represents not only latent heating but also heating due to subgrid-scale processes. Latent heating due to large-scale condensation (hereafter called "condensation" for brevity) is equal to $-c_p/L_v$ times the specific humidity tendency due to large-scale condensation. This parameterization scheme adjusts the specific humidity to its saturation value when it is exceeded within a grid box. The latent heating due to convection is calculated as a relaxation toward an equilibrium profile (see section 2b). Latent heating from diffusion describes the vertical mixing of temperature in the boundary layer, using a Monin–Obukhov scheme (more details are given in Frierson et al. 2006).

We examine the response of latent heating and specific humidity tendency due to advection (defined in section 3c) to warming in two ranges of parameters. In the first range, presented in Fig. 6, the eddy-driven jet shifts in opposite directions in the T42 and T85 simulations (the same range of parameters examined in section 5b). In the second range, presented in Fig. 7, the eddy-driven jet shifts poleward with warming for both T42 and T85 resolutions. In Fig. 7, the baseline simulation is with $CO_2 = 300$ ppm and HF = 0.9, while the warmer simulation uses $CO_2 = 300$ ppm and HF = 1.1. This comparison allows us to examine whether the direction of the eddy-driven jet shift is related to changes in the moisture budget.

For the range of parameters in which the eddy-driven jet shifts equatorward with warming in the T42 simulations (Fig. 6), it can be observed that the contribution of latent heating to the diabatic heating response [Figs. 6c(1),c(2)] is greater than that of radiation [Figs. 6b(1),b(2)]. In the T42 simulations, the diabatic heating is strengthened and shifted upward [Fig. 6a(1)], whereas in the T85 simulations, the diabatic heating is shifted upward and poleward [Fig. 6a(2)] with comparatively less strengthening (Figs. 5c,f). The radiative heating is negative almost everywhere in the midlatitude midtroposphere in an approximately homogeneous pattern below 400 hPa and shows a weak and mostly negative response to warming [Figs. 6b(1),b(2)]. The maximum latent heating is concentrated over the midlatitude (40°–50°N) midtroposphere [500–700 hPa, Figs. 6c(1),c(2)]. Similar to the response of diabatic heating, latent heating is strengthened and shifted upward using T42 where an upward and poleward shift of

latent heating is observed in the T85 simulations [Figs. 6c(1),c(2)]. The specific humidity tendency due to advection is dominated by the contribution from eddy moisture flux convergence (not shown). The specific humidity tendency due to advection strengthens and shifts upward in the T42 simulations, but shifts upward and poleward in the T85 simulations [Figs. 6d(1),d(2)]. It is weaker than the latent heating response, especially in the T42 simulations, which means that the latent heating response is not only due to changes in humidity tendency due to advection. We will return to this point in the next subsection.

Figure 7 shows the case where the circulation shifts poleward in response to climate change for both resolutions. With both resolutions, the diabatic heating is concentrated at the boundary layer in the cooler simulation and shifts upward and poleward in response to warming [Figs. 7a(1),a(2)]. The radiative heating spreads nearly homogeneously in the midlatitude midtroposphere and does not contribute much to the diabatic heating response in this region [Figs. 7b(1),b(2)], similar to the case shown in Figs. 6b(1) and 6b(2). The latent heating contributes much to the diabatic heating and is concentrated near 44°N at the boundary layer and shifts upward and poleward [Figs. 7c(1),c(2)]. The specific humidity tendency due to advection also shows a poleward and upward shift using both resolutions [Figs. 7d(1),d(2)], but its response is weaker than the latent heating response. The similarity between the diabatic heating terms response in the two resolutions for this range of parameters is consistent with the similar eddy-driven jet shifts. This supports the assumption that the diabatic heating response and the direction of the eddy-driven jet shift are connected.

The results so far indicate that a strengthening of the diabatic heating in the midlatitude midtroposphere is related to an equatorward shift of the eddy-driven jet, whereas an upward and poleward shift of midlatitude diabatic heating is related to a poleward shift of the eddy-driven jet. The decomposition in Figs. 6 and 7 shows that the different responses of midlatitude diabatic heating in the two cases are due to differences in the latent heating response. However, this response cannot be attributed only to differences in humidity advection, since latent heating, parameterized by condensation, convection, and diffusion schemes, is stronger than the temperature tendency associated with specific humidity advection.

e. Relationship between heating due to specific humidity tendency and latent heating

The motivation for this subsection is to examine which terms contribute to the response of latent heating, after the previous subsection showed that it is not explained by humidity advection alone. We focus on the set of simulations showing opposite shifts of the eddy-driven jet in response to warming in the T42 and T85 simulations (the same set of simulations examined in Figs. 4 and 6). All the left column of each block in Fig. 8 shows the specific humidity source terms and the right column presents the components of the latent heating (i.e., the temperature tendency from the respective
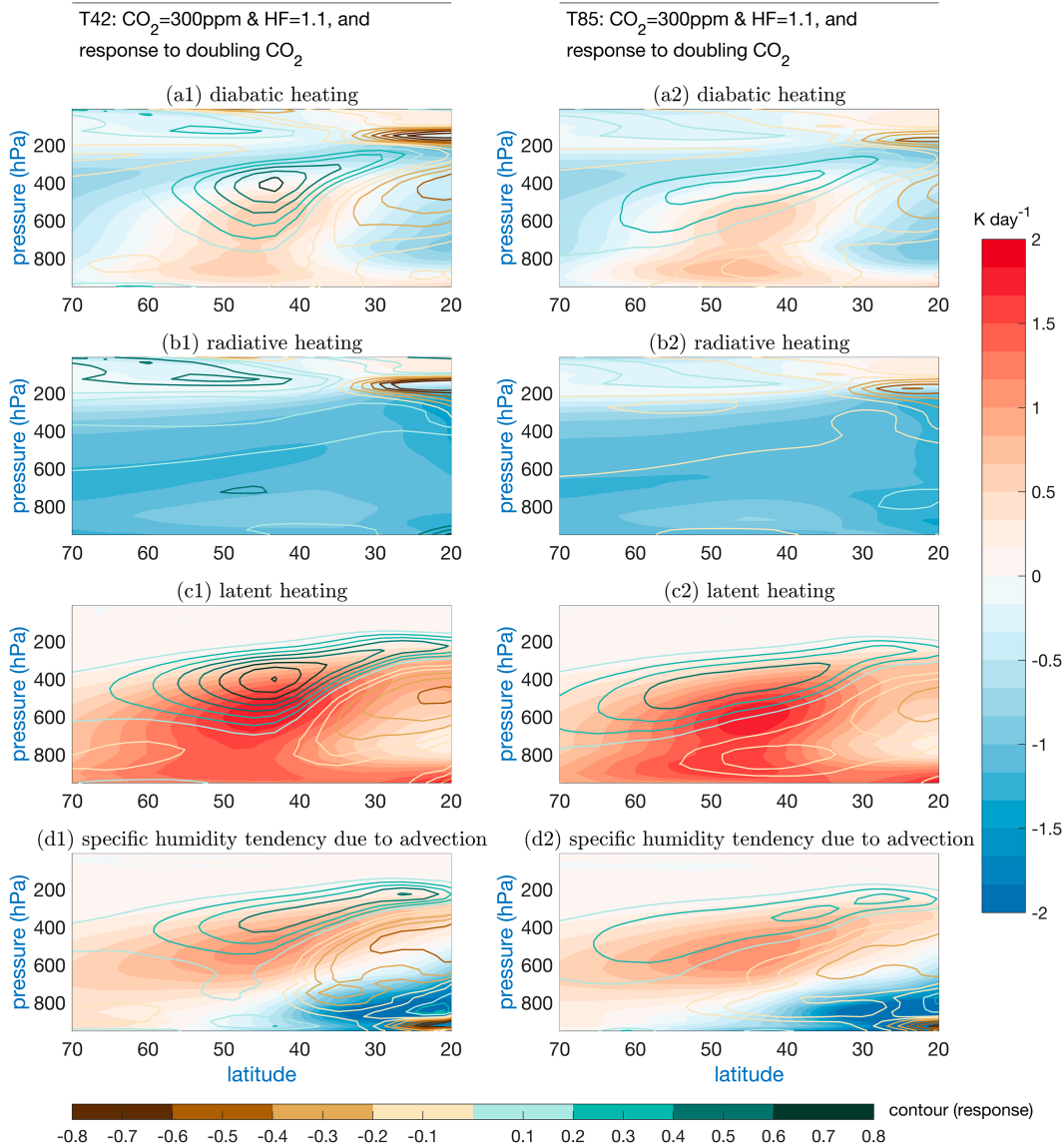
FIG. 6. DH terms using (left) T42 and (right) T85 resolutions in the idealized GCM for the cooler simulation (shaded; using CO_2 = 300 ppm and HF = 1.1), where the terms are (a1),(a2) total DH, (b1),(b2) radiative heating, (c1),(c2) latent heating, and (d1),(d2) L_v/c_p times the specific humidity tendency due to advection. The solid colored contours represent the changes in response to warming (where the parameters in the warmer simulation are CO_2 = 600 ppm and HF = 1.1). All the plots are in units of K day^{-1}.

parameterization scheme). The sum of the specific humidity source terms is represented by $\bar{S}$ in Eq. (4). In a statistically steady state, where the left-hand side of Eq. (4) is zero, $\bar{S}$ is equal to minus the total specific humidity tendency due to advection (examined in the previous subsection). To ease the comparison between the specific humidity terms and the latent heating terms, the humidity tendency terms are multiplied by $-L_v/c_p$ [Figs. 8d(1) and 8d(3) shows $\bar{S}$, multiplied by $-L_v/c_p$, which is similar to the total humidity tendency from advection shown in Figs. 6d(1) and 6d(2), respectively]. A negative specific humidity tendency term means that the water vapor is condensed and latent heating is released, so that

$-L_v/c_p$ times this term represents the amount of latent heating release associated with this term. The left block represents the model simulations with T42 resolution where the T85 simulations are placed in the right block.

Most of the latent heating response in the midtroposphere comes from convection and large-scale condensation [for both resolutions, Figs. 8a(2),a(4),b(2),b(4)]. Both the terms have comparable contributions in terms of the strength of the response. In the convection terms, there is a large difference between the humidity tendency [Figs. 8a(1),a(3)] and heating [Figs. 8a(2),a(4)], where the positive heating response in the midtroposphere, which is much stronger in the T42 than the
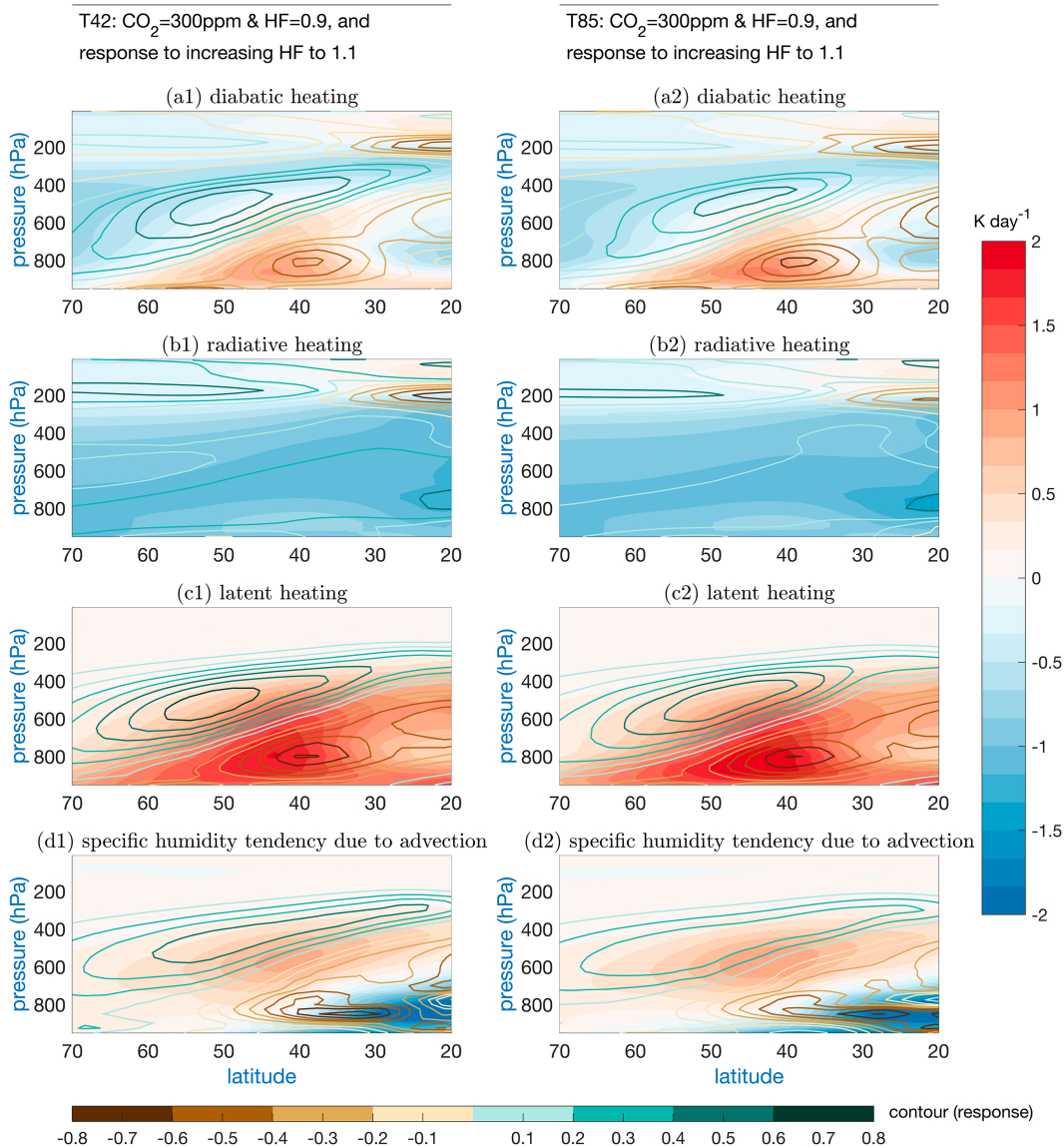
T42: CO$_2$=300ppm & HF=0.9, and
response to increasing HF to 1.1

T85: CO$_2$=300ppm & HF=0.9, and
response to increasing HF to 1.1

FIG. 7. As in Fig. 6, but for the cooler simulation using CO$_2$ = 300 ppm and HF = 0.9 (colored shading) and the warmer simulation using CO$_2$ = 300 ppm and HF = 1.1 (the response to warming is shown in colored contours).

T85 simulations, does not appear in the humidity tendency term. In the large-scale condensation terms, humidity tendency [Figs. 8b(1),b(3)] and heating [Figs. 8b(2),b(4)] are exactly the same, as defined by the large-scale condensation scheme. The diffusion terms are negligible over the midtroposphere but large at the boundary layer for both the specific humidity tendency and latent heating [Figs. 8c(1)–c(4)]. In the boundary layer, convection, diffusion, and large-scale condensation are all important, with the former two contributing to the difference between the specific humidity tendency due to advection and latent heating in the midlatitude boundary layer (Figs. 6c,d). The sum of the contributions from all parameterizations shows a much larger midtropospheric heating response in the T42 simulation [Fig. 8d(2)] than in the T85 simulation [Fig. 8d(4)], while the difference in the

humidity tendency response between the resolutions is milder [Figs. 8d(1),d(3)], as noted above in the discussion of Fig. 6. Overall, Fig. 8 shows that the main difference in the diabatic heating response between the T42 and T85 simulations, associated with the different jet shifts (as shown in the previous subsections), comes from the convective heating term and is not associated with the specific humidity tendency due to convection. Note that the convection scheme in the model is designed to conserve moist enthalpy in the vertical integral, but not locally for each level, so that latent heating and humidity tendency due to convection can be locally different (see section 2b and Frierson 2007).

Recent studies by Fuchs et al. (2023) and Garfinkel et al. (2024) point to a major role of differences in the convection scheme in the intermodel spread of the jet latitude and its

T42: CO_2=300ppm & HF=1.1, and response to doubling CO_2

T85: CO_2=300ppm & HF=1.1, and response to doubling CO_2
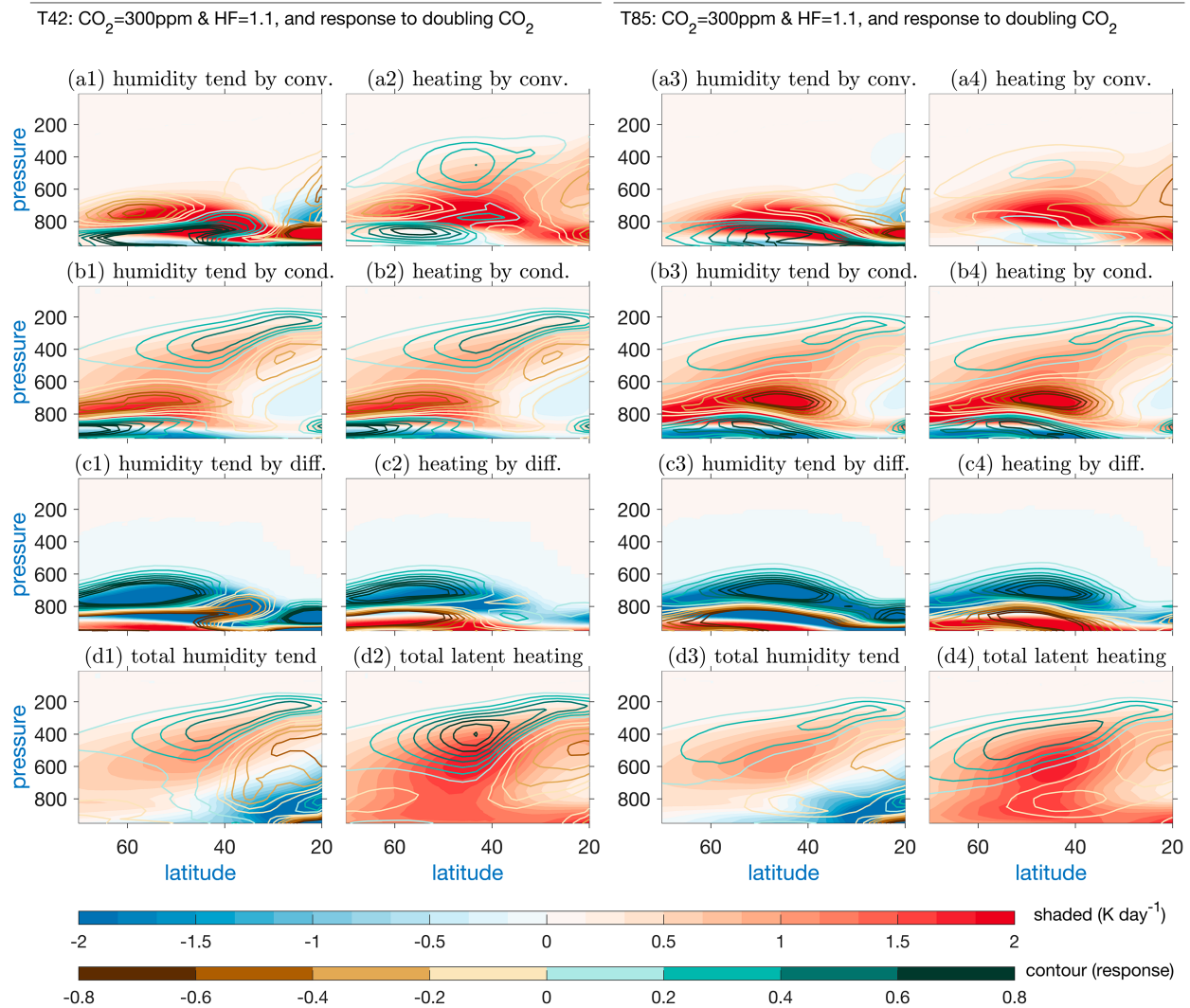

FIG. 8. Decomposition of latent heating terms and specific humidity source terms (multiplied by $-L_v/c_p$) using T42 resolution in the first block and T85 resolution in the second block in the idealized GCM under the cooler climate (color shading; experiment with CO_2 = 300 ppm and HF = 1.1) and in response to climate change (colored contours; the difference between the experiment with CO_2 = 600 ppm and HF = 1.1 and the cooler experiment). (a1)–(a4) Tendency due to convection, (b1)–(b4) tendency due to condensation, (c1)–(c4) tendency due to diffusion, and (d1)–(d4) total tendency due to latent heating and specific humidity source, for the respective model resolution. The positive values of the moisture tendency terms correspond to drying because they are multiplied by $-L_v/c_p$. Units are in K day^{-1}.

response to climate change in comprehensive climate models and idealized atmospheric models. The study of Fuchs et al. (2023) shows that a model with only deep convection tends to produce a more equatorward jet, whereas a model with shallow convection tends to produce a more poleward jet in the SH summer. They find a similar relationship in an idealized atmospheric model and in comprehensive climate models. The study of Garfinkel et al. (2024) uses the same model as in this study (MiMA; see section 2b) to examine the effect of different versions of the convective parameterization on the eddy-driven jet shift. They find that when shallow convection is turned off, the preindustrial simulation exhibits a more equatorward jet compared to a case with shallow convection. Furthermore, they find a poleward jet shift in response to

climate change in the absence of shallow convection and no significant shift when shallow convection is included. The results presented here support the conclusions of these studies that there is a relation between convective heating and the jet latitude in models. Specifically, we find that parameterized convective heating plays a major role in the midlatitude diabatic heating response. We provide a theoretical framework for connecting the diabatic heating response to the eddy-driven jet shift.

f. The momentum budget

As noted in the previous subsections, increasing the resolution in our simulations affects both the diabatic heating and the eddy-driven jet latitude. The momentum budget could provide some insight into how the eddy-driven jet latitude
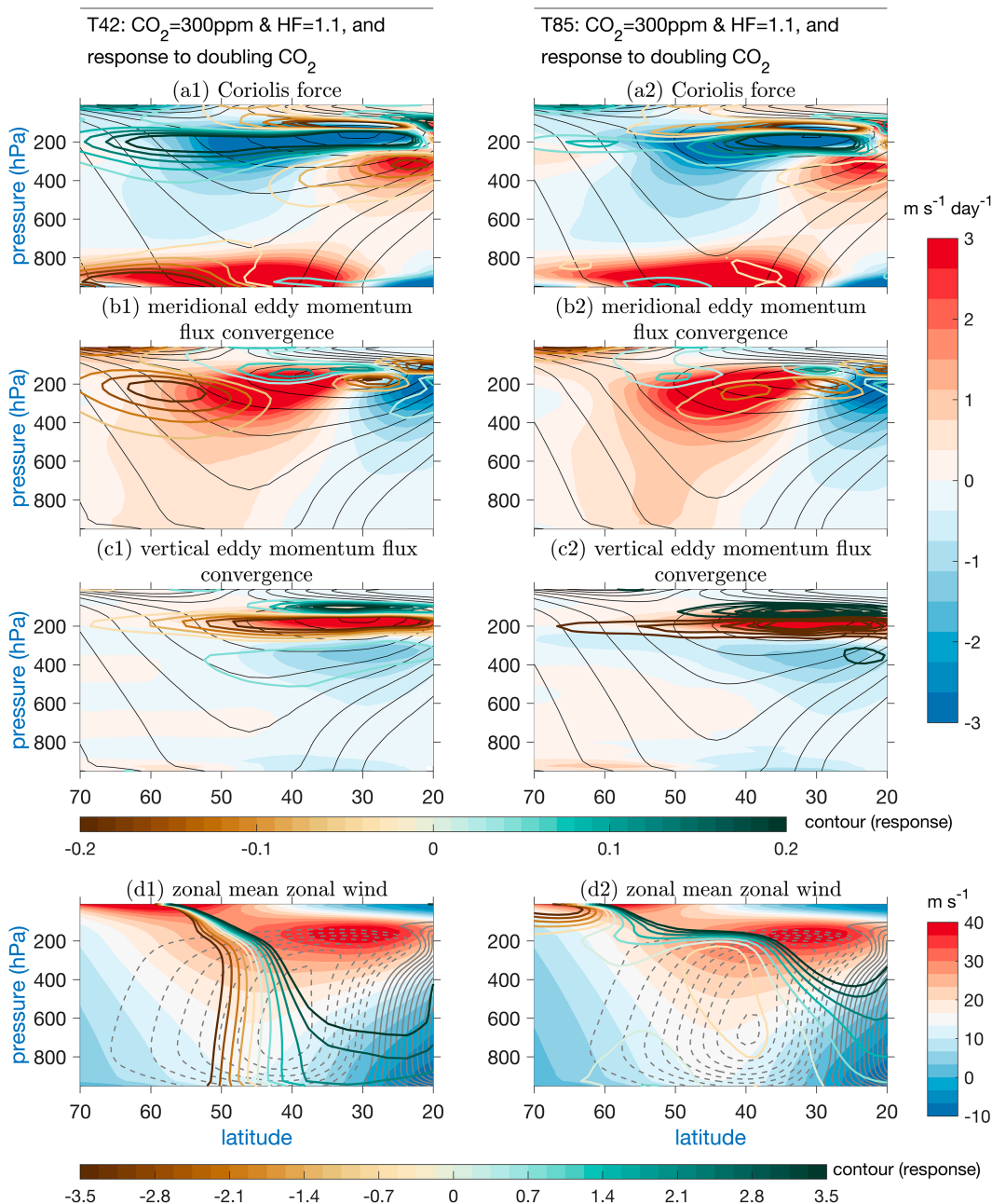
FIG. 9. Midlatitude momentum budget terms and zonal wind in the idealized GCM. The shaded colors show the (a1),(a2) Coriolis force, (b1),(b2) meridional eddy momentum flux convergence, (c1),(c2) vertical eddy momentum flux convergence, and (d1),(d2) zonal wind (m s^{-1}) in the cooler climate (as in Fig. 6) for the (left) T42 simulations and (right) T85 simulations. The black contours in (a1)–(c2) represent the zonal wind (m s^{-1}) where the contour interval is 5 m s^{-1} starting from zero. The gray contours in (d1) and (d2) represent the mass streamfunction with the contour interval of 5×10^9 kg s^{-1}. The colored contours represent the difference between the warmer and cooler simulations.

changes with resolution. In this subsection, we examine what changes in the momentum budget are related to the equatorward shift of the jet in the T42 simulations and how they are different from the T85 simulations. The momentum budget is calculated using Eq. (5). Figure 9 shows the major momentum budget terms (defined in section 3d) for the same simulations

considered in Figs. 4, 6, and 8, along with the zonal-mean zonal wind. The terms of meridional and vertical momentum advection by the mean flow are relatively small in the midlatitudes and are not shown in Fig. 9.

The structure of the Coriolis term is consistent with the structure of the circulation cells [Figs. 9a(1),a(2), compared

with the streamfunction in Fig. 4], with positive Coriolis force in the Hadley cell and negative Coriolis force in the Ferrel cell in the upper troposphere (around 300 hPa). The response of the Coriolis force in the upper branch of the Ferrel cell in the T42 simulations [Fig. 9a(1)] is positive and extended to high latitudes. This response is consistent with a weakening of the Ferrel cell and the appearance of a polar cell at high latitudes (positive Coriolis force at high latitudes is consistent with a polar cell which appears in the warmer T42 simulation poleward of around 55°N, refer to Fig. 4e). In contrast, in the T85 simulations, a weak response of the Coriolis force at high latitudes is observed [Fig. 9a(2)], consistent with the weak response of the mass streamfunction at high latitudes (Figs. 4i,m).

The meridional eddy momentum flux convergence and its response to warming are shown in Figs. 9b(1) and 9b(2). In the T42 resolution experiment (Fig. 9b1), the eddy momentum flux response decelerates the zonal wind at the poleward side of the jet, consistent with the equatorward shift of the jet [Figs. 3b(2) and 9d(1)]. The appearance of the eddy momentum flux divergence on the poleward side of the jet in the T42 experiment is consistent with the appearance of the polar cell, since the eddy momentum flux convergence term and the Coriolis term nearly balance each other in this region. In contrast, no such deceleration is seen on the poleward side of the jet in the T85 simulations [Fig. 9b(2)], and consistently, there is no equatorward shift of the jet [Figs. 3b(4) and 9d(2)]. The vertical eddy momentum flux does not contribute significantly to the momentum budget response, except for an upward response on the equatorward side of the jet [Figs. 9c(1),c(2)]. Explaining the differences in the responses of the eddy momentum flux convergence between the two resolutions is beyond the scope of this work. We note that these results show a connection between the differences in the diabatic heating responses and the differences in the eddy momentum flux responses, since they are both linked to the Ferrel cell becoming narrower and a polar cell appearing in the T42 resolution, in contrast with the absence of this response in the T85 resolution.

The zonal-mean zonal wind shows an equatorward shift in response to warming in the T42 simulations as seen by the positive values on the equatorward side and the negative values on the poleward side of the jet [Fig. 9d(1)]. In the T85 simulations, the response of the zonal-mean zonal wind around the eddy-driven jet latitude is very weak [Fig. 9d(2)], as the shift of the jet is nearly stagnated in this range of parameters [see Fig. 3b(4)].

6. Summary and conclusions

This study examines the relation between the response of midlatitude diabatic heating and the response of the midlatitude circulation to climate change, with a focus on the latitudinal shift of the eddy-driven jet. Some studies investigating the latitudinal shift of the eddy-driven jet in response to climate change have assumed that the jet shifts together with the eddy heat flux and the baroclinic zone (e.g., Frierson 2008; Lu et al. 2008; Butler et al. 2011; Voigt and Shaw 2016). Other studies explained the eddy-driven jet shift from considerations of wave propagation properties that change due to increased

zonal winds in the upper troposphere and lower stratosphere (e.g., Chen et al. 2008; Rivière 2011; Lorenz 2014). However, the role of midlatitude diabatic heating in the eddy-driven jet response to climate change has not been systematically examined yet. Recent studies indicate that there is a negative correlation between the eddy-driven jet latitude and the strength of midlatitude midtropospheric diabatic heating in the interannual variability in observations (Lachmy and Kaspi 2020) and in the intermodel variability in climate models (Lachmy 2022). Based on the heat and momentum budgets, these studies showed that stronger diabatic heating is associated with a larger latitudinal separation between the eddy-driven jet and eddy heat flux, which can explain this negative correlation.

Here, we examine the relevance of the theoretical framework suggested by Lachmy and Kaspi (2020) for the eddy-driven jet shift in response to climate change. According to this framework (see section 1), the latitudes of maximum midtropospheric poleward eddy heat flux and the eddy-driven jet (defined by the maximum surface westerlies) are collocated if three conditions are satisfied: 1) The maximum eddy heat flux is collocated with the maximum of the Ferrel cell streamfunction. This condition is satisfied if midlatitude midtropospheric diabatic heating is negligible. 2) The maximum Ferrel cell streamfunction is collocated with the maximum meridional wind in the lower branch of the Ferrel cell. This condition depends on the geometric structure of the Ferrel cell. 3) The maximum meridional wind in the lower branch of the Ferrel cell is collocated with the maximum surface westerlies. This condition depends on the near-surface momentum balance. If all three conditions are approximately satisfied, then the eddy-driven jet is expected to shift together with the eddy heat flux in response to climate change. However, if the strength of midlatitude midtropospheric diabatic heating is significantly changed in response to climate change, this will affect condition 1 and may lead to a decoupling between the eddy heat flux and eddy-driven jet shifts.

The poleward shift of the eddy heat flux and other storm-track metrics is a robust response to climate change in models of different complexity levels (see review by Shaw et al. 2016). In contrast, a few studies found an equatorward shift of the eddy-driven jet in response to climate change, under certain model parameters (Pfahl et al. 2015; Dwyer and O'Gorman 2017; Lachmy and Shaw 2018; Tan et al. 2019; Davis and Birner 2022). While the poleward shift of the eddy heat flux can be directly connected to the increased surface temperature by a relatively simple theoretical argument (viz., the stabilization on the equatorward side of the storm track due to increased static stability, e.g., Frierson 2008), the explanations suggested for the eddy-driven jet shift are linked to the surface temperature in a more complicated chain of causation (see review by Shaw 2019). By examining CMIP6 data for the SH summer, we show here that the intermodel spread in the eddy heat flux latitude is strongly correlated with the mean midlatitude surface temperature. However, the eddy-driven jet latitude is not significantly correlated with the mean midlatitude surface temperature, when considering the intermodel spread within each experiment. We argue that this lack of significant correlation is at least partly due to the intermodel variability in the strength of midlatitude

The midlatitude atmospheric circulation response to climate change

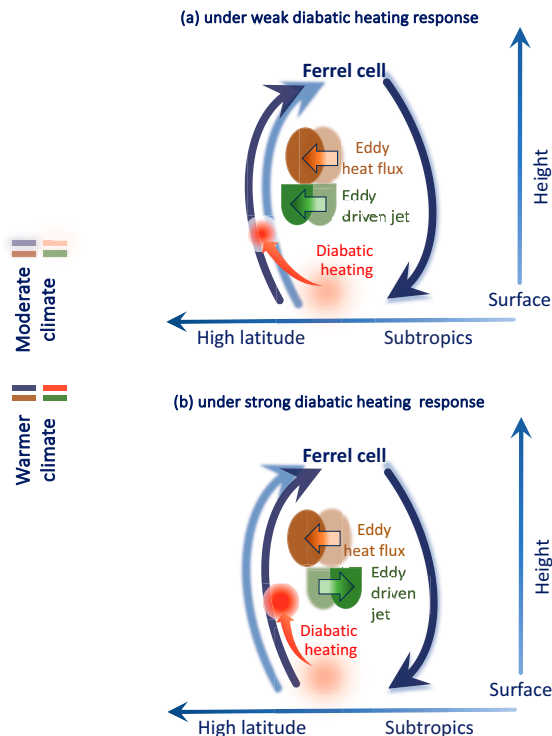**(a) under weak diabatic heating response**

FIG. 10. Schematic diagram of two different midlatitude circulation responses to warming: (a) a case where midlatitude DH shifts upward and poleward and slightly strengthens and (b) a case where midlatitude DH sharply increases and shifts upward in the midtroposphere. In case (a), the EDJ and the Ferrel cell streamfunction shift poleward with the EHF in response to climate change, whereas in case (b), the EDJ and the Ferrel cell rising branch shift equatorward, while the EHF shifts poleward. The relation between the DH response and the EDJ shift is explained based on the heat and momentum balance constraints (see text).

midtropospheric diabatic heating, which affects the latitudinal separation between the eddy heat flux and eddy-driven jet (Lachmy 2022).

To further investigate the relation between the responses of midlatitude diabatic heating and the eddy-driven jet to warming, we use an idealized aquaplanet model (MiMA; Jucker and Gerber 2017), where a wide range of climates is obtained. The climate in the model is modified by increasing the CO_2 concentration and by increasing the humidity factor, which is a nondimensional parameter multiplying the saturation vapor pressure in the Clausius–Clapeyron equation. We find that the atmospheric circulation in the model depends on the mean surface saturation vapor pressure, which increases with the CO_2 concentration and the humidity factor. The response of the midlatitude circulation to climate change (induced by increased saturation vapor pressure) differs when the model resolution is increased from T42 to T85.

The response of the midlatitude circulation and diabatic heating to climate change in the two cases found using the idealized model is described schematically in Fig. 10. The first

case (Fig. 10a) describes what is found using the T85 resolution for all the parameter sweep. Midlatitude diabatic heating shifts upward and poleward with climate change, increasing gradually in the midtroposphere [Figs. 3d(4) and 5e,f]. The eddy heat flux, eddy-driven jet, and Ferrel cell streamfunction shift monotonically poleward [Figs. 3a(4),b(4),c(4)]. In this case, the cooling by the Ferrel cell ascending branch is balanced partly by eddy heat flux convergence and partly by diabatic heating in both climates (Figs. 4i,j,l–n,p). This means that condition 1 from Lachmy and Kaspi (2020) is not changed significantly between the two climates. This heat budget response allows for the Ferrel cell to shift together with the eddy heat flux. The eddy-driven jet shifts with the Ferrel cell due to the Ferrel cell structure and the momentum balance condition [conditions 2 and 3 from Lachmy and Kaspi (2020)].

The second case (Fig. 10b) describes what is found using the T42 resolution for the intermediate range of climates. The diabatic heating shifts upward and strengthens sharply in the midtroposphere in response to climate change [Figs. 3d(2) and 5b,c]. The eddy heat flux shifts poleward, but the Ferrel cell streamfunction and the eddy-driven jet shift equatorward [Figs. 3a(2),b(2),c(2)]. The strong midlatitude diabatic heating in the warmer climate balances most of the cooling by the Ferrel cell ascending branch, while at higher latitudes, diabatic cooling is balanced mostly by eddy heat flux convergence (Figs. 4e,f,h). In this case, condition 1 from Lachmy and Kaspi (2020) is not satisfied in the warmer climate. The response of the heat budget terms allows for the Ferrel cell ascending branch to shift in the opposite direction to the eddy heat flux shift. The eddy-driven jet shifts with the Ferrel cell streamfunction, consistent with conditions 2 and 3. These considerations explain the opposite shifts of the eddy heat flux and eddy-driven jet in this case.

Even though the coarser-resolution simulations are farther from capturing the realistic phenomena, the basic theoretical explanations for the jet response to climate change are expected to apply for these cases as well. We therefore use them as test cases for challenging the theoretical arguments that predict a poleward shift of the eddy-driven jet in response to climate change. Furthermore, an equatorward shift of the jet in response to climate change was also found in simulations using T85 resolution (Pfahl et al. 2015).

The explanation given above argues for a connection between the response of midlatitude diabatic heating to climate change and the direction of the eddy-driven jet shift, but it does not imply any causal relation. Since midlatitude diabatic heating is dominated by latent heat release associated with midlatitude storms (Fig. 6), it is strongly coupled to the eddy momentum flux that drives the eddy-driven jet and is associated with the same storms. However, the model parameterizations of convective and boundary layer mixing (diffusion) processes, which we refer to as components of the latent heating, are not locally identical to the latent heating associated with the humidity tendency terms because they represent also the effect of subgrid-scale processes. The latent heating associated with the humidity tendency terms in the model is found to contribute only weakly to the total latent heating (Figs. 6

and 7), and it is found that convective heating plays a dominant role in the strengthening of the midlatitude midtropospheric diabatic heating between the moderate and warmer climates in the T42 simulations (Fig. 8). We are therefore unable to point to the direct causal link between the diabatic heating response and the response of midlatitude storms to climate change in the model.

The sensitivity of the results to the model resolution could be related to the convective parameterization (e.g., Frierson 2007; Herrington and Reed 2017) or to the wavebreaking processes that are not represented well when the model resolution is low (e.g., Jablonowski and Williamson 2006; Lu et al. 2015). We find that the equatorward jet shift in the T42 experiment is accompanied by the appearance of a polar cell and strong eddy momentum flux divergence at high latitudes, which does not occur using the T85 resolution (Fig. 9). The momentum balance between the Coriolis force and the eddy momentum flux convergence in the upper troposphere requires that this high-latitude momentum flux divergence would be accompanied by the appearance of a polar cell. On the other hand, the appearance of the polar cell is also consistent with the equatorward shift of the Ferrel cell, which in turn is related to the response of the heating by the Ferrel cell that balances the strong midlatitude diabatic heating. In this sense, we show a connection between the sensitivity of the diabatic heating and eddy momentum flux to the model resolution, but we are unable to determine causal relations.

These results imply that the representation of the eddy-driven jet and its response to climate change in climate models depends, among other factors, on the parameterizations of latent heating processes and specifically convective parameterizations. Recent studies found that the latitude of the eddy-driven jet is sensitive to the inclusion of shallow convection in the convective parameterization in comprehensive climate models (Fuchs et al. 2023) and in the idealized model used here, MiMA (Garfinkel et al. 2024). In the model simulations presented here, the direction of the eddy-driven jet shift in response to climate change is linked to the response of convective heating in the midlatitude midtroposphere. We argue here that when trying to explain or evaluate the eddy-driven jet shift in response to climate change, based on idealized or comprehensive climate models, the factors controlling the diabatic heating response should also be taken into account, since the midlatitude diabatic heating and the eddy-driven jet latitude are mutually constrained through the heat and momentum balance conditions.

REFERENCES

Barnes, E. A., and L. Polvani, 2013: Response of the midlatitude jets, and of their variability, to increased greenhouse gases in the CMIP5 models. *J. Climate*, **26**, 7117–7135, https://doi.org/10.1175/JCLI-D-12-00536.1.

Betts, A. K., 1986: A new convective adjustment scheme. Part I: Observational and theoretical basis. *Quart. J. Roy. Meteor. Soc.*, **112**, 677–691, https://doi.org/10.1002/qj.49711247307.

——, and M. J. Miller, 1986: A new convective adjustment scheme. Part II: Single column tests using GATE wave, BOMEX, ATEX and Arctic air-mass data sets. *Quart. J. Roy. Meteor. Soc.*, **112**, 693–709, https://doi.org/10.1002/qj.49711247308.

Butler, A. H., D. W. J. Thompson, and R. Heikes, 2010: The steady-state atmospheric circulation response to climate change–like thermal forcings in a simple general circulation model. *J. Climate*, **23**, 3474–3496, https://doi.org/10.1175/2010JCLI3228.1.

——, ——, and T. Birner, 2011: Isentropic slopes, downgradient eddy fluxes, and the extratropical atmospheric circulation response to tropical tropospheric heating. *J. Atmos. Sci.*, **68**, 2292–2305, https://doi.org/10.1175/JAS-D-10-05025.1.

Chang, E. K. M., Y. Guo, and X. Xia, 2012: CMIP5 multimodel ensemble projection of storm track change under global warming. *J. Geophys. Res.*, **117**, D23118, https://doi.org/10.1029/2012JD018578.

Chen, G., J. Lu, and D. M. W. Frierson, 2008: Phase speed spectra and the latitude of surface westerlies: Interannual variability and global warming trend. *J. Climate*, **21**, 5942–5959, https://doi.org/10.1175/2008JCLI2306.1.

——, ——, and L. Sun, 2013: Delineating the eddy–zonal flow interaction in the atmospheric circulation response to climate forcing: Uniform SST warming in an idealized aquaplanet model. *J. Atmos. Sci.*, **70**, 2214–2233, https://doi.org/10.1175/JAS-D-12-0248.1.

Curtis, P. E., P. Ceppi, and G. Zappa, 2020: Role of the mean state for the Southern Hemispheric jet stream response to CO_2 forcing in CMIP6 models. *Environ. Res. Lett.*, **15**, 064011, https://doi.org/10.1088/1748-9326/ab8331.

Davis, N. A., and T. Birner, 2022: Eddy-mediated Hadley cell expansion due to axisymmetric angular momentum adjustment to greenhouse gas forcings. *J. Atmos. Sci.*, **79**, 141–159, https://doi.org/10.1175/JAS-D-20-0149.1.

Dwyer, J. G., and P. A. O'Gorman, 2017: Moist formulations of the Eliassen–Palm flux and their connection to the surface westerlies. *J. Atmos. Sci.*, **74**, 513–530, https://doi.org/10.1175/JAS-D-16-0111.1.

Frierson, D. M. W., 2007: The dynamics of idealized convection schemes and their effect on the zonally averaged tropical

circulation. *J. Atmos. Sci.*, **64**, 1959–1976, https://doi.org/10.1175/JAS3935.1.

——, 2008: Midlatitude static stability in simple and comprehensive general circulation models. *J. Atmos. Sci.*, **65**, 1049–1062, https://doi.org/10.1175/2007JAS2373.1.

——, I. M. Held, and P. Zurita-Gotor, 2006: A gray-radiation aquaplanet moist GCM. Part I: Static stability and eddy scale. *J. Atmos. Sci.*, **63**, 2548–2566, https://doi.org/10.1175/JAS3753.1.

Fuchs, D., S. C. Sherwood, D. Waugh, V. Dixit, M. H. England, Y.-L. Hwong, and O. Geoffroy, 2023: Midlatitude jet position spread linked to atmospheric convective types. *J. Climate*, **36**, 1247–1265, https://doi.org/10.1175/JCLI-D-21-0992.1.

Garfinkel, C. I., I. White, E. P. Gerber, M. Jucker, and M. Erez, 2020: The building blocks of Northern Hemisphere wintertime stationary waves. *J. Climate*, **33**, 5611–5633, https://doi.org/10.1175/JCLI-D-19-0181.1.

——, B. Keller, O. Lachmy, I. White, E. P. Gerber, M. Jucker, and O. Adam, 2024: Impact of parameterized convection on the storm track and near-surface jet response to global warming: Implications for mechanisms of the future poleward shift. *J. Climate*, **37**, 2541–2564, https://doi.org/10.1175/JCLI-D-23-0105.1.

Gerber, E. P., S. Voronin, and L. M. Polvani, 2008: Testing the annual mode autocorrelation time scale in simple atmospheric general circulation models. *Mon. Wea. Rev.*, **136**, 1523–1536, https://doi.org/10.1175/2007MWR2211.1.

Guemas, V., and F. Codron, 2011: Differing impacts of resolution changes in latitude and longitude on the midlatitudes in the LMDZ atmospheric GCM. *J. Climate*, **24**, 5831–5849, https://doi.org/10.1175/2011JCLI4093.1.

Held, I. M., and B. J. Soden, 2006: Robust responses of the hydrological cycle to global warming. *J. Climate*, **19**, 5686–5699, https://doi.org/10.1175/JCLI3990.1.

Herrington, A. R., and K. A. Reed, 2017: An explanation for the sensitivity of the mean state of the community atmosphere model to horizontal resolution on aquaplanets. *J. Climate*, **30**, 4781–4797, https://doi.org/10.1175/JCLI-D-16-0069.1.

Holton, J. R., 2004: *An Introduction to Dynamic Meteorology*. Academic Press, 535 pp.

Iacono, M. J., E. J. Mlawer, S. A. Clough, and J.-J. Morcrette, 2000: Impact of an improved longwave radiation model, RRTM, on the energy budget and thermodynamic properties of the NCAR community climate model, CCM3. *J. Geophys. Res.*, **105**, 14 873–14 890, https://doi.org/10.1029/2000JD900091.

Jablonowski, C., and D. L. Williamson, 2006: A baroclinic instability test case for atmospheric model dynamical cores. *Quart. J. Roy. Meteor. Soc.*, **132**, 2943–2975, https://doi.org/10.1256/qj.06.12.

Jucker, M., and E. P. Gerber, 2017: Untangling the annual cycle of the tropical tropopause layer with an idealized moist model. *J. Climate*, **30**, 7339–7358, https://doi.org/10.1175/JCLI-D-17-0127.1.

Kidston, J., and E. P. Gerber, 2010: Intermodel variability of the poleward shift of the austral jet stream in the CMIP3 integrations linked to biases in 20th century climatology. *Geophys. Res. Lett.*, **37**, L09708, https://doi.org/10.1029/2010GL042873.

——, G. K. Vallis, S. M. Dean, and J. A. Renwick, 2011: Can the increase in the eddy length scale under global warming cause the poleward shift of the jet streams? *J. Climate*, **24**, 3764–3780, https://doi.org/10.1175/2010JCLI3738.1.

Lachmy, O., 2022: The relation between the latitudinal shifts of midlatitude diabatic heating, eddy heat flux, and the eddy-driven jet in CMIP6 models. *J. Geophys. Res. Atmos.*, **127**, e2022JD036556, https://doi.org/10.1029/2022JD036556.

——, and T. Shaw, 2018: Connecting the energy and momentum flux response to climate change using the Eliassen–Palm relation. *J. Climate*, **31**, 7401–7416, https://doi.org/10.1175/JCLI-D-17-0792.1.

——, and Y. Kaspi, 2020: The role of diabatic heating in Ferrel cell dynamics. *Geophys. Res. Lett.*, **47**, e2020GL090619, https://doi.org/10.1029/2020GL090619.

Lin, P., Y. Ming, and T. Robinson, 2023: On the resolution sensitivity of equatorial precipitation in a GFDL global atmospheric model. *J. Adv. Model. Earth Syst.*, **15**, e2022MS003300, https://doi.org/10.1029/2022MS003300.

Lorenz, D. J., 2014: Understanding midlatitude jet variability and change using Rossby wave chromatography: Poleward-shifted jets in response to external forcing. *J. Atmos. Sci.*, **71**, 2370–2389, https://doi.org/10.1175/JAS-D-13-0200.1.

Lu, J., G. Chen, and D. M. W. Frierson, 2008: Response of the zonal mean atmospheric circulation to El Niño versus global warming. *J. Climate*, **21**, 5835–5851, https://doi.org/10.1175/2008JCLI2200.1.

——, ——, and ——, 2010: The position of the midlatitude storm track and eddy-driven westerlies in aquaplanet AGCMs. *J. Atmos. Sci.*, **67**, 3984–4000, https://doi.org/10.1175/2010JAS3477.1.

——, ——, L. R. Leung, D. A. Burrows, Q. Yang, K. Sakaguchi, and S. Hagos, 2015: Toward the dynamical convergence on the jet stream in aquaplanet AGCMs. *J. Climate*, **28**, 6763–6782, https://doi.org/10.1175/JCLI-D-14-00761.1.

Maher, P., and Coauthors, 2019: Model hierarchies for understanding atmospheric circulation. *Rev. Geophys.*, **57**, 250–280, https://doi.org/10.1029/2018RG000607.

O'Gorman, P. A., and T. Schneider, 2008a: Energy of midlatitude transient eddies in idealized simulations of changed climates. *J. Climate*, **21**, 5797–5806, https://doi.org/10.1175/2008JCLI2099.1.

——, and ——, 2008b: The hydrological cycle over a wide range of climates simulated with an idealized GCM. *J. Climate*, **21**, 3815–3832, https://doi.org/10.1175/2007JCLI2065.1.

Pfahl, S., P. A. O'Gorman, and M. S. Singh, 2015: Extratropical cyclones in idealized simulations of changed climates. *J. Climate*, **28**, 9373–9392, https://doi.org/10.1175/JCLI-D-14-00816.1.

Pope, V., and R. Stratton, 2002: The processes governing horizontal resolution sensitivity in a climate model. *Climate Dyn.*, **19**, 211–236, https://doi.org/10.1007/s00382-001-0222-8.

Rivière, G., 2011: A dynamical interpretation of the poleward shift of the jet streams in global warming scenarios. *J. Atmos. Sci.*, **68**, 1253–1272, https://doi.org/10.1175/2011JAS3641.1.

Shaw, T. A., 2019: Mechanisms of future predicted changes in the zonal mean mid-latitude circulation. *Curr. Climate Change Rep.*, **5**, 345–357, https://doi.org/10.1007/s40641-019-00145-8.

——, and Z. Tan, 2018: Testing latitudinally dependent explanations of the circulation response to increased CO_2 using aquaplanet models. *Geophys. Res. Lett.*, **45**, 9861–9869, https://doi.org/10.1029/2018GL078974.

——, and Coauthors, 2016: Storm track processes and the opposing influences of climate change. *Nat. Geosci.*, **9**, 656–664, https://doi.org/10.1038/ngeo2783.

Simpson, I. R., and L. M. Polvani, 2016: Revisiting the relationship between jet position, forced response, and annular mode variability in the southern midlatitudes. *Geophys. Res. Lett.*, **43**, 2896–2903, https://doi.org/10.1002/2016GL067989.

——, K. A. McKinnon, F. V. Davenport, M. Tingley, F. Lehner, A. Al Fahad, and D. Chen, 2021: Emergent constraints on the large-scale atmospheric circulation and regional hydroclimate:

Do they still work in CMIP6 and how much can they actually constrain the future? *J. Climate*, **34**, 6355–6377, https://doi.org/10.1175/JCLI-D-21-0055.1.

Tamarin, T., and Y. Kaspi, 2017: The poleward shift of storm tracks under global warming: A Lagrangian perspective. *Geophys. Res. Lett.*, **44**, 10 666–10 674, https://doi.org/10.1002/2017GL073633.

Tan, Z., and T. A. Shaw, 2020: Quantifying the impact of wind and surface humidity-induced surface heat exchange on the circulation shift in response to increased CO$_2$. *Geophys. Res. Lett.*, **47**, e2020GL088053, https://doi.org/10.1029/2020GL088053.

——, O. Lachmy, and T. A. Shaw, 2019: The sensitivity of the jet stream response to climate change to radiative assumptions. *J. Adv. Model. Earth Syst.*, **11**, 934–956, https://doi.org/10.1029/2018MS001492.

Vallis, G. K., P. Zurita-Gotor, C. Cairns, and J. Kidston, 2015: Response of the large-scale structure of the atmosphere to global warming. *Quart. J. Roy. Meteor. Soc.*, **141**, 1479–1501, https://doi.org/10.1002/qj.2456.

Voigt, A., and T. A. Shaw, 2016: Impact of regional atmospheric cloud radiative changes on shifts of the extratropical jet stream in response to global warming. *J. Climate*, **29**, 8399–8421, https://doi.org/10.1175/JCLI-D-16-0140.1.